

# 1.2-million-year band of Earth–Mars obliquity modulation on the evolution of cold late Miocene to warm early Pliocene climate

Jie Qin<sup>1</sup>, Rui Zhang<sup>1</sup>, Vadim Kravchinsky<sup>2</sup>, Jean-Pierre Valet<sup>3</sup>, Leonardo Sagnotti<sup>4</sup>, Jianxing Li<sup>5</sup>, Yong Xu<sup>6</sup>, Taslima Anwar<sup>1</sup>, and Leping Yue<sup>1</sup>

<sup>1</sup>Northwest University

<sup>2</sup>University of Alberta

<sup>3</sup>Institut de Physique du Globe de Paris

<sup>4</sup>Istituto Nazionale di Geofisica e Vulcanologia

<sup>5</sup>Chengdu Center of Geological Survey, Geological Survey of China

<sup>6</sup>Xi'an Center of Geological Survey, China Geological Survey

November 22, 2022

## Abstract

The climatic transitions during the Miocene–Pliocene epochs had significant impacts on the worldwide biological diversity and were associated with large turnovers of continental vegetation and fauna. Previous studies have shown that late Miocene cooling and continental aridification which was initiated 7 Ma reversed to warm conditions across the Miocene–Pliocene Boundary  $\sim$  5.3 Ma. Here we present detailed orbital pacing of Asian monsoon deposits to constrain further the global climate change during this period. We produce high-resolution magnetic susceptibility records which reveal that the 1.2 Myr obliquity modulation would have been the main driving factor of the cooling and warming that occurred  $\sim$  7 Ma and 5.3 Ma, respectively. The Tibetan rise and closures of the Panama and Indonesian seaways enhanced the impact of the 405 kyr eccentricity cycles to an oscillatory climatic state while the Northern Hemisphere glaciations were increasing from 4 to 2.5 Ma.

**1.2-million-year band of Earth–Mars obliquity modulation on the  
evolution of cold late Miocene to warm early Pliocene climate**

Jie Qin<sup>1,2</sup>, Rui Zhang<sup>1,2\*</sup>, Vadim A. Kravchinsky<sup>1,2,\*</sup>, Jean-Pierre Valet<sup>1,3</sup>, Leonardo  
Sagnotti<sup>4</sup>, Jianxing Li<sup>5</sup>, Yong Xu<sup>6</sup>, Taslima Anwar<sup>1,2</sup>, Leping Yue<sup>1</sup>

<sup>1</sup> Institute of Cenozoic Geology and Environment, State Key Laboratory of Continental  
Dynamics, Department of Geology, Northwest University, 710069 Xi'an, China

<sup>2</sup> Geophysics, Department of Physics, University of Alberta, T6G2E1 Edmonton, Canada

<sup>3</sup> Institut de Physique du Globe de Paris, 75238 Paris cedex 05, France

<sup>4</sup> Istituto Nazionale di Geofisica e Vulcanologia, 00143 Roma, Italy

<sup>5</sup> Chengdu Center of Geological Survey, Geological Survey of China, 610081 Chengdu,  
China

<sup>6</sup> Xi'an Center of Geological Survey, China Geological Survey, 710054 Xi'an, China

\* e-mails: [ruizhang@nwu.edu.cn](mailto:ruizhang@nwu.edu.cn) (R.Z.), [vadim@ualberta.ca](mailto:vadim@ualberta.ca) (V.A.K.)

16   **Abstract**

17   The climatic transitions during the Miocene–Pliocene epochs had significant impacts on  
18   the worldwide biological diversity and were associated with large turnovers of  
19   continental vegetation and fauna. Previous studies have shown that late Miocene cooling  
20   and continental aridification which was initiated 7 Ma reversed to warm conditions  
21   across the Miocene–Pliocene Boundary ~ 5.3 Ma. Here we present detailed orbital  
22   pacing of Asian monsoon deposits to constrain further the global climate change during  
23   this period. We produce high-resolution magnetic susceptibility records which reveal  
24   that the 1.2 Myr obliquity modulation would have been the main driving factor of the  
25   cooling and warming that occurred ~ 7 Ma and 5.3 Ma, respectively. The Tibetan rise  
26   and closures of the Panama and Indonesian seaways enhanced the impact of the 405 kyr  
27   eccentricity cycles to an oscillatory climatic state while the Northern Hemisphere  
28   glaciations were increasing from 4 to 2.5 Ma.

29

30   astrochronology; Chinese Loess Plateau; grand obliquity modulation;  
31   magnetostratigraphy; Miocene-Pliocene; red clay

32

## 1. Introduction

In the late Miocene, terrestrial environments and ecosystems have undergone tremendous changes due to the presumed decline of atmospheric CO<sub>2</sub> between 8 and 6 Ma (Beerling et al., 2011; Bolton and Stoll, 2013). This period has seen the replacement of large areas of tropical and subtropical forests by deserts (such as Sahara and Taklimakan Deserts) and the expansion of C4 grassland (Cerling et al., 1997; Schuster et al., 2006; Huang et al., 2007). The large restructuring of vegetation and landscape coincided with major turnovers in animal communities (Badgley et al., 2008). However, those continental environmental upheavals do not bring direct information on the temperature change during the Late Miocene (Herbert et al., 2016). The marine isotope record younger than the middle Miocene is characterized by periodic anomalies of the Antarctic ice volume that have been shown to be probably driven by obliquity in marine sequences from the peri-Antarctic margin (Naish et al., 2009). No clear trend suggests a long-term climatic change during the late Miocene (Zachos et al., 2001; Lewis et al., 2008; Westerhold et al., 2020). Recently, the integration of marine sea-surface temperature (SST) made it possible to estimate the evolution of global temperature during the Miocene (LaRiviere et al., 2012; Herbert et al., 2016). The late Miocene cooling did not lead monotonically to the ice age in the northern hemisphere that prevailed through most of the Pliocene (LaRiviere et al., 2012). Furthermore, temperature proxies indicate that cooling and aridification ceased during the Pliocene and that warmer conditions occurred after 5.3 Ma (Ravelo et al., 2004; Dowsett et al., 2005; Fedorov et al., 2006; Lawrence et al., 2006). Because the present-day global warming may induce Pliocene-like temperatures during the next decades, a good



knowledge of the transition from a cold late-Miocene and warm early-middle Pliocene climate may provide a valuable analog for climatic projections (Burke et al., 2018).

It remains uncertain whether there is a link between contemporaneous atmospheric circulation, ecosystem changes in continental environments and the orbital variation effects recorded by climate proxies from the ocean realm. The hundreds of thousand-years' time scale low-latitude processes such as monsoon forcing on the upper-ocean circulation and its productivity strongly influences climate dynamics and constrains the reconstruction of ice volume and atmospheric greenhouse gas concentrations (Holbourn et al., 2018). The high topography of the Tibetan-Pamir Plateau contributes to amplify the Asian monsoon system that controls precipitation as well as the level of convection (An et al., 2001; Boos and Kuang, 2010). During the Quaternary, the climate was mostly affected by low-amplitude variability of precessional insolation modulated by the 405 and 100 kyr eccentricity cycles and the 41 kyr obliquity band (Nie et al., 2008; Hao et al., 2012; Nie, 2018; Sun et al., 2019). In earlier records from late Miocene to Pliocene, some may show unconventional cycles related to the orbital inclination rates of Earth and Saturn, called 173 kyr metronome for Asian monsoon, arouses our interest (Zhang et al., 2022). From analysis of the obliquity solution, both the 173 kyr and 1.2 Myr obliquity bands are of particular importance, the signal from the second is even much stronger than that of the first one (Laskar, 2020). In order to detect the longer orbitally forced cycle that has not been studied in the monsoon region, and to estimate whether it is associated with critical late Miocene-Pliocene climate transitions, we choose the eolian red clay deposits as the research subject.

78

## 79   **2. Material and methods**

### 80   **2.1 Material**

81   The monsoonal system is primarily characterized by intense summer rainfall over a wide  
82   area which lies along the continental-ocean pressure gradient and brings rainfall onto the  
83   continent (An et al., 2001; Sun et al., 2019). The East Asian monsoon (EAM) controls  
84   the amounts of precipitation and dust brought from the Indian to the Pacific Ocean by  
85   seasonal changes of warm moist air. Dry winds from the Asian high latitudes at high  
86   elevations transported dust that yielded the formation of the Chinese Loess Plateau (CLP)  
87   (Hao et al., 2012) ([Figure 1a](#)). The Liulin (LL) eolian red clay section (N37°21',  
88   E110°45') is flanked to the east by the Luliang Mountains and to the west by the Yellow  
89   River, dozens of kilometers away from the large mountain ridges ([Figure 1b](#)). The 68-  
90   meter thick wind-blown deposits consist of brownish red clay with sporadic and smaller  
91   caliche nodules (<5 cm) and abundant Fe–Mn coatings at the top intercalated by  
92   carbonate horizons. The bottom of the wind-blown deposits in the LL section was dated  
93   late Miocene by comparing the *Hipparion* teeth discovered at 56.3 m in the LL section  
94   with the analogous fossil layers in the neighbouring Fugu and Baode sections (Xue et al.,  
95   1995; Zhang et al., 1995; Zhu et al., 2008; Xu et al., 2013). This constraint enabled us to  
96   establish a first chronology of the LL section after correlating the magnetostratigraphic  
97   data to the geomagnetic polarity timescale (GPTS) (Ogg, 2012).

98

## 99    **2.2 Methods**

### 100    **2.2.1 Sampling and Laboratory Measurements**

101

102    30 samples at 2 m stratigraphic spacing were selected for thermomagnetic analyses using  
103    a MFK2 Kappabridge with a CS-4 furnace under an argon atmosphere to prevent  
104    oxidation during heating. Oriented paleomagnetic samples ~ every 10 cm and cut into 2  
105    cm thick cubes for paleomagnetic measurements. A total of 618 samples were measured  
106    at 20 cm, increased to 10 cm in the parts where polarity reversals were more frequent.  
107    The samples were stepwise demagnetized every 50°C from room temperature up to  
108    600°C using an MMTD 80 thermal demagnetizer. The natural remanent magnetization  
109    was measured using either a spinner JR6-A magnetometer or a 2G-755 magnetometer  
110    located in a low magnetic field space (<100 nT). The directions of the characteristic  
111    remanent magnetization were estimated by principal component analysis (Kirschvink,  
112    1980). Only determinations with maximum angular deviation (MAD) below 10° were  
113    accepted.

114    The magnetic susceptibility (MS) of powdered samples was measured using a Bartington  
115    MS-2 susceptibility meter. Grain size (GS) analysis was performed with a Mastersizer  
116    2000 laser particle analyzer. 0.2 g powder samples were first treated with 10% H<sub>2</sub>O<sub>2</sub> for  
117    about 15 min to remove organic matter and to ensure that the excess peroxide was  
118    destroyed. Carbonate was removed using 10% boiling HCl solution of 10ml and the  
119    samples were dispersed for 15 min. with 10 ml 10% Na(PO<sub>3</sub>)<sub>6</sub> in an ultrasonic bath prior  
120    to the measurements. We performed a cyclostratigraphy analysis through spectral

analysis of the MS and GS stratigraphic trends. We repeated the procedure to generate several new correlations between the magnetic polarity zones and the GPTS till the orbital periods were resolved clearly in the MS and GS stratigraphic trends.

### **2.2.2 Spectral Analysis**

Spectral analysis was applied to check the occurrence of Milankovitch periodicities in MS and GS trends by attempting several correlations between each magnetic polarity pattern and the GPTS (Anwar et al., 2015; Zhang et al., 2021). Wavelet analysis with 95% confidence level of background red noise was used to calculate the spectra of the MS and GS records (Torrence and Compo, 1998). Before spectral analysis, we removed the long-term trends by subtracting a fitted smooth line in order to minimize the effects of non-orbital periods. We established an initial magnetostratigraphy and then generated several correlation patterns between each magnetic polarity pattern and the GPTS until the best orbital bands were clearly observed. After confirming the magnetostratigraphy, both 405-kyr and 100-kyr cycles were extracted by filtering bands at the same time (with two bandwidths of 350–500 kyr and 80–125 kyr separately) in Matlab. Coherence between the band-pass filtered MS and eccentricity was scrutinized by calculating a correlation coefficient between the two-time series at zero phase using Matlab codes throughout the late Miocene – early and middle Pliocene. We shifted the MS curve towards younger or older ages by ~ 30 to 200 kyr steps that were imposed by the coherency analysis in order to maximize the coherency between the two-time series with zero-time lag; then, a

new time series could be obtained from the tuning process. The process was repeated many times until each peak of the two curves matched well and the correlation coefficient at zero-time lag reached the maximum. Midway in the process, for a very small time lag between the two series, we stretched or squeezed the MS curve manually to make it match the eccentricity. Each tuned timescale was also applied to GS records at the same time. The spectral powers were produced to help determine our final age model.

### 3. Results

#### 3.1 Rock magnetism and magnetostratigraphy

The plots of MS ( $\chi$ ) versus temperature (T) show that the heating and cooling cycles are nearly reversible (Figure 2). The sharp drop of  $\chi$  between ~400–585 °C, indicates the presence of magnetite. Further decrease of  $\chi$  to 700 °C reveals that hematite is also present. Representative demagnetization results for different depths are shown in Figure 3 with orthogonal vector diagrams. Our demagnetization results demonstrated that the low-temperature overprints generally ranged from the room temperature to 200 °C. After the elimination of the low-temperature component, the samples yielded a stable characteristic remanent magnetization (ChRM) tending to the origin.

Paleomagnetic analysis reveals five normal (N1 – N5) and five reversed (R1 – R5) polarity intervals from the reliable ChRM directions (Figure 4). All magnetostratigraphic

intervals are established based on more than 4 coinciding samples (and over at least 0.8 meters in the depth) to excluded the effects from small amplitude and short period anomalies (Zhang et al., 2018; Zhang, Kravchinsky, et al., 2021, Zhang, Wei, et al., 2021 Zhang et al., 2022). Three brief normal polarity events (less than or equal to 4 coinciding samples and less than 0.8 m in thickness) were also verified from the ChRM recording (red horizons in [Figure 3](#)). Sand, gravel and mammalian fossils found in the lower part of the section show negligible significant influence from alluvial processes ([Figure 4a](#)). The dense carbonate layers and mud-stone suggest that during the ongoing uplift of the Lvliang Mountains, groundwater was of interest from time to time because it could re-magnetize large amounts of wind-blown sediments. We marked five such prominent layers with light green shading in [Figure 4](#).

The fossils found from sandy layers at 56.3 m in depth of the section containing the *Hipparion* fauna were dated between 7.2 and 6.8 Ma at adjacent Fuxing section, 7.0–6.7 Ma at the Wujiamao and Baode sections (Zhu et al., 2008; Xu et al., 2013; Zhang et al., 2022). Here, *Hipparion* teeth are thought to be ~ 6.8 Ma in the magnetostratigraphy when N5 and R5 are correlated to C3An and C3Br. This constraint enabled us to establish a first chronology after correlating the magnetostratigraphic data to the geomagnetic polarity timescale (GPTS) (Ogg, 2012). Following the visual correlation, N1 – N3 are associated with C3n.1n – C3n.3n while a brief normal event remains a question mark with respect to C3n.4n. In the field observation, dense calcareous nodules, mudstone and carbonate layers developed from 18 – 27 m, which means underneath the short polarity record at ~18 m, records of rising groundwater flows had been continuously superimposed in the stratum from 27 m and above. Such rework could have

disrupted the original paleomagnetism, causing the remagnetization to obscure the previous record. The lower two events at ~ 60 m from the section are only recorded in the sandy layer. As paleomagnetic samples in sand are likely acquired viscous magnetic fields through remagnetization, further verification of the authenticity is required for these question marked red horizons (Zhang et al., 2018; Zhang, Kravchinsky et al., 2021; Zhang, Wei, et al., 2021; Zhang et al., 2022). Considering that there are dense carbonate and sandy layers at the depth of 41-46 m, it indicates that groundwater might also affect the remnant magnetization of the N4 polarity zone. In this case, only N1, N2, N3 and N5 can be used for the initial targeting age prior to tuning to the orbital parameters. Then, we performed a cyclostratigraphy analysis through spectral analysis of the MS and GS records. To verify the correctness of our magnetostratigraphic correlation we generated several new correlations between the magnetic polarity zones and the GPTS and performed spectral analysis until the orbital periods were clearly resolved in the MS and GS records. Clear peaks of the 405 kyr eccentricity band can be observed between 7 and 5.4 Ma (Figure. 5A and 5C). The 100 kyr cycles can also be identified at around 6.2–6 Ma in the MS spectrum even though their power amplitudes were much weaker than the 405 kyr power (Figure 5A). Analogously, a relatively low-amplitude 100 kyr cycles revealed between 5.9 and 5.7 Ma in the GS spectrum (Figure 5C). The final magnetostratigraphic correlation that incorporated the cyclostratigraphic procedure described in Methods is shown in Figure 4.

### 3.2 Orbital tuning and astronomical calibration

209

210 Once the magnetostratigraphic age of the LL section has been compatible with the  
211 cyclostratigraphy, we conducted two-channel-band filtering (405 kyr and 100 kyr) for  
212 both MS and GS data to highlight the visibility of the eccentricity band and tunes the  
213 filtered record cycle-by-cycle to the long eccentricity maxima (405 kyr) and short  
214 eccentricity maxima (100 kyr) at the same time (Figure 5). To examine the coupling  
215 between our records and eccentricity cycles, we calculated the correlation coefficient  
216 between filtered MS and eccentricity at zero phase. Then we shifted the filtered MS  
217 curve to the left or right at a short time span implied by the coherency analysis in order  
218 to fit it with the filtered eccentricity 405 kyr until the correlation coefficient was  
219 maximized. After that we carried out fine adjustments to the stronger 100 kyr cycle  
220 improving further the correlation coefficient. We repeated this procedure until the curve  
221 matching and correlation coefficients were maximized. During the tuning processes, we  
222 also adjusted some small time lags between the two series, by stretching or squeezing the  
223 MS peaks to the eccentricity peaks (Figure 5B). The final astronomical calibration based  
224 on the MS tuning was applied to the GS record (Figure 5D).

225 The calculated sedimentation rate (Figure 6) varied from 1.6 to 3.6 cm/kyr with an  
226 average of 2.2 cm/kyr. These values are typical of the eolian red clay dust in the CLP  
227 (e.g. Nie et al., 2008; Anwar et al., 2015; Zhang et al., 2018).

228

### 229 3.3 Stratigraphic correlations

230



To investigate large-scale climate variations we first compare the LL section to the classical Jingchuan section (JC) which is located in the middle of CLP (Ding et al., 2001), and the adjacent Shilou (SL) section which is situated close to LL and stratigraphically continues LL to the younger age until 2.6 Ma (Ding et al., 2001; Anwar et al., 2015) ([Figure 7](#)). Further Comparisons to the eastern and western edges of CLP can be found in [Supplementary Fig. 1](#).

The bottom age of the SL section was extensively debated and assigned from the late Miocene at 11 Ma (Xu et al., 2009, 2012), 8 Ma (Ao et al., 2016; 2018), to the early Pliocene at 5.2 Ma (Anwar et al., 2015; Zhang, et al., 2018, 2022). Both Xu et al. (2012) and Ao et al. (2016, 2018) mistakenly assigned the finding of micromammal *Meriones* sp. at a depth of 46.6 m in the SL section to correspond to the Miocene age. However, the original studies of Zheng et al. (2000, 2001) cited by Ao et al. (2016, 2018) did not confirm that the *Meriones* sp. belonged to the Miocene. Zheng et al., (2000, 2001) established that another micromammal *Pseudomeriones* sp. existed in the Miocene, whereas *Meriones* sp. lived during the Pliocene and Pleistocene (Dianat et al., 2017). Therefore the chronology presented in Anwar et al. (2015) and Zhang et al. (2018, 2022) is consistent with the Pliocene-Pleistocene age for the SL section. We note that the bottom of the SL red clay is not exposed in the outcrop and in the future it is possible to reach the late Miocene red clay layers using drilling. The LL section is older than the SL section considering the fossil evidence from both SL and LL that is supported by the magnetostratigraphy.

The LL section is located in a valley with a lower elevation compared to the SL section and has ~ 400 m height difference with 40 km horizontal separation of the sections

(Figure 1b). Taking it into account we combined both records that have overlap between each other into a long magnetic susceptibility (LMS) record spanning from the Gauss chron to C3A chron (Figure 7). Both MS records were stacked together by averaging the values between two parts in the overlapping interval of 5.2 – 4 Ma. Figure 7 demonstrates similarities of the general long-term trends between LMS and the JC section MS record (Ding et al., 2001), while smaller scale features differ in the terms of amplitudes.

## 4. Discussion

### 4.1 Discovery of the 1.2 Myr cycle in the Asian monsoon record

The typical changes of MS records in the eolian sediments of CLP are well known for their close match with the global ice-interglacial cycles depicted by the  $\delta^{18}\text{O}$  records in marine sediments and by the time-series of summer insolation at 65° N derived from orbital solutions (Laskar et al., 2004). We obtained independent climate records from terrestrial archives of CLP in order to reconstruct the atmospheric circulation in eastern Asia since the late Miocene. We compared our stacked LMS record from the eastern part of CLP with the inland JC red clay section (Figure 7a-d) (Ding et al., 2001).

The results of the wavelet analysis of the LMS record show a clear 405 kyr eccentricity cycle between 7 and 2.5 Ma (Figure 7e) which is linked to the gravitational interaction of Jupiter and Venus (g2–g5), while the MS in the central CLP indicates an accentuation of

the 405 kyr band between 4 and 2.5 Ma (Figure 7f). Interestingly, a ~1.2 Myr grand cycle of  $s_4 - s_3$  obliquity modulation, linked to the orbital inclination rates of Mars and Earth, is superimposed with the 405 and 100 kyr bands (Figure 7e & 7f) similarly to previous climatic records (van Dam et al., 2006) and is interpreted as beats between secular frequencies  $p+s_4$  and  $p+s_3$  (Laskar et al., 2004). The chaotic solar system has two major secular resonances. The first argument,  $\theta = (s_4 - s_3) - 2 (g_4 - g_3)$  draws particular attention because the two longest orbital secular frequencies, obliquity and precession modulations, from  $s_4 - s_3$  and  $g_4 - g_3$  (~2.4 Myr) experienced intermittent chaotic transitions at ~ 2:1 resonance states, when ~1.2 Myr cycle dominates since 50 Ma (Hinnov, 2000; Laskar et al., 2004; Palike et al., 2004; Crampton et al., 2018).

To further highlight the expression of the 405 and 100 kyr eccentricity bands within the LMS and JS records, we applied a two-channel band-pass filter with 350–500 kyr and 80–125 kyr bandwidths, respectively (red curves in Figure 8) after removing the long-term trend that could be related to tectonic processes in the region (Anwar et al., 2015; R. Zhang, Kravchinsky, et al., 2021; Zhang et al., 2022). The minima of each 405 kyr cycle after the filter application between ~5.3 Ma and 2.5 Ma for both MS curves (Figure 8d & 8e) correlate with the eccentricity maxima (Figure 8c). However, prior to this period the curves are out of phase suggesting that some other signal should have affected the climate variations during the late Miocene. In contrast to the filtered signals and astronomical cycles (red solid and green dashed lines), the unfiltered MS (Fig. 8d, f) curves show less variability but the conspicuous grand cycle related to the 1.2 Myr obliquity modulation is evident between 7.1 and 4 Ma.

## 4.2 Global documentation of the 1.2 Myr cycle that drives the Miocene-Pliocene climate variations

Obliquity, precession and their modulations have been shown to be important driving forces of the global monsoon system which is sensitive to change in insolation, waxing and waning of ice sheets and CO<sub>2</sub> concentration (Prell and Kutzbach, 1992; Nie et al., 2008; Anwar et al., 2015; Nie, 2018; Zhang et al., 2022). Various time series, such as MS,  $\delta^{18}\text{O}$ , SST and atmospheric CO<sub>2</sub> levels, display a significant climatic transition at ~5.3 Ma (Beerling et al., 2011; Herbert et al., 2016; Holbourn et al., 2018; Tian et al., 2008; Liu et al., 2019) (Fig. 9). The MS records show that the intensification of the Tibetan Plateau rise enhanced the 405 kyr band by a strengthened summer monsoon since ~ 3.6 – 4.2 Ma (Fig. 9b, c) (Nie et al., 2008). Therefore, we suggest that tectonic processes that impacted regional land-sea heat exchanges influenced strongly the orbital-sensitive climate fluctuations, which, in turn, induced significant changes in the insolation-forced summer monsoon and led to introducing the tectonic related long-term trend towards two-three times higher values of MS in the interval between ~ 4.2 and 3.6 Ma (Fig. 9b, c). In the ocean, the negative shifts of benthic  $\delta^{18}\text{O}$  records (Fig. 9d) correspond to the increase of MS (Fig. 9b, c) that is consistent with a dominant summer monsoon regime linked to a global warming at 5.3 Ma (Holbourn et al., 2018). In contrast, the positive shifts of  $\delta^{18}\text{O}$  (Fig. 9d) and the decrease of MS (Fig. 9b, c) and SST (Fig. 9h) correspond to a global cooling and inland aridification that led to the birth of the Sahara and Taklimakan deserts ~ 7 Ma (Schuster et al., 2006; Sun et al., 2009).

Previous studies have pointed out that a strengthened winter monsoon during the 7.1–5.5 Ma time interval was associated with an expansion of ice sheets in the Northern Hemisphere (Wolf-Welling et al., 1996; Thiede et al., 1998; Holbourn et al; 2018) and indicated a global cooling during the late Miocene (Zachos et al., 2001). The  $\delta^{18}\text{O}$  record of benthic foraminifera showed a clear decrease indicating a warming transition ~5.5 – 5.3 Ma. (Holbourn et al; 2018; Westerhold et al., 2020). A stronger deep-sea ventilation could have constrained warmer and saline surface water to flow up to the high-latitude North Pacific and Atlantic subtropical gyres and thus deliver additional heat and moisture to the Northern Hemisphere that contributed to a global warming 5.3 Ma. Such interpretation of both climatic variations at ~7 and 5.3 Ma is supported by the variability of the 1.2 Ma obliquity modulation (Fig. 9a & Fig. 10) during the 7.6 – 3.6 Ma intervals. The grand obliquity curve is on the descent at 7 Ma and on the rise at 5.3 Ma.

Several lines of evidence indicate that the closure of the Panama and Indonesia seaways may have also caused a significant reorganization of ocean circulation and increased the Gulf Stream yielding substantial transfer of warm and saline water masses to high northern latitudes during the Miocene-Pliocene between 6 and 2.7 Ma (Cane et al., 2001; Haug et al., 2001; Molnar, 2008). The warm conditions at high latitudes (Fig. 9f) may result from the massive input of warmer water. The planktonic foraminifera isotopic records from the Caribbean Sea indicate that salinity of the Caribbean surface waters already started to increase at the beginning of Pliocene, suggesting a weakened surface water circulation between the tropical Atlantic and Pacific Oceans as a result of the growth of the Central American isthmus of Panama (Haug et al., 1998). It probably led to a climate pattern of a 405-kyr cycle in the western Hemisphere even earlier than the

Asian Monsoon region (Fig. 9g) (Nie, 2018). However, there is still controversy, to determine when the seaway closed, if not possible, until the “Great American Exchange” of Vertebrates between North and South America that occurred  $\sim 2.7 - 2.6$  Ma (Molnar, 2008). On the other hand, the thickening of the equatorial Western Pacific warm pool triggered by the closure of the Panama and Indonesian seaways may have expanded the exchanges of heat and moisture toward high latitudes. This process contributed to warming up of the South China Sea water and to increasing the precipitation on the Asian continent (Yan et al., 1992; Li et al., 2008). The gradual growth of the Tibetan Plateau  $\sim 4.2$  Ma may have also increased the air pressure gradient between land and sea, resulting in greater seasonal precipitation within the monsoon influence region. The 1.2 and 0.405 Myr long amplitude modulations of the obliquity and precession cycles are prominent features of the climate pattern between the late Miocene and Pliocene, especially for the Asian monsoon.

## 5. Conclusions

Our interpretation of the LMS record shows that the Asian summer monsoon appears to be orbitally controlled by the 1.2 Myr grand obliquity cycle band between 7.7 and 4 Ma and by the 0.405 Myr long eccentricity band between 4 and 2.5 Ma. We conclude that global cooling and warming that occurred 7 and 5.3 Ma respectively, as well as the Antarctic ice volume, carbon cycle dynamics and the monsoon forcing of the upper-ocean circulation were all triggered by the grand obliquity variations before the middle Pliocene. Since then, a series of major tectonic events such as the closure of the Panama

and Indonesian seaways and the uplift of the Tibetan Plateau, accelerated the transition from a 1.2 Myr obliquity-dominated to a 0.405 Myr eccentricity-dominated climate variability for the Asian monsoon.

## **Acknowledgments**

This study was funded by the National Natural Science Foundation of China (41772027, 41972035 and 41950410574) for R.Z., J.Q. and J.L., the China Scholarship Council for J.Q., and the Natural Sciences and Engineering Research Council of Canada (NSERC grant RGPIN-2019-04780) for V.A.K. The data related to the manuscript will be available at <https://zenodo.org> after the manuscript is accepted for publication. We temporarily upload the data to the supplementary file for review.

## **Competing Interests**

The authors declare no competing interests.

## **References**

384 An, Z., Kutzbach, J.E., Prell, W.L., Porter, S.C., 2001. Evolution of Asian monsoons and  
 385 phased uplift of the Himalaya–Tibetan plateau since Late Miocene times. *nature*  
 386 411, 62–66.

387 Anwar, T., Kravchinsky, V.A., Zhang, R., 2015. Magneto-and cyclostratigraphy in the  
 388 red clay sequence: New age model and paleoclimatic implication for the eastern  
 389 Chinese Loess Plateau. *Journal of Geophysical Research: Solid Earth*, 120, 6758–  
 390 6770.

391 Ao, H., Roberts, A.P., Dekkers, M.J., Liu, X., Rohling, E.J., Shi, Z., An, Z., Zhao, X.,  
 392 2016. Late Miocene–Pliocene Asian monsoon intensification linked to Antarctic  
 393 ice-sheet growth. *Earth and Planetary Science Letters* 444, 75–87.

394 Badgley, C., Barry, J.C., Morgan, M.E., Nelson, S.V., Behrensmeyer, A.K., Cerling,  
 395 T.E., Pilbeam, D., 2008. Ecological changes in Miocene mammalian record show  
 396 impact of prolonged climatic forcing. *Proceedings of the National Academy of*  
 397 *Sciences*, 105, 12145–12149.

398 Beerling, D.J., Royer, D.L., 2011. Convergent Cenozoic CO<sub>2</sub> history. *Nature Geoscience*  
 399 4, 418–420.

400 Bolton, C.T., Stoll, H.M., 2013. Late Miocene threshold response of marine algae to  
 401 carbon dioxide limitation. *Nature* 500, 558–562.

402 Boos, W.R., Kuang, Z., 2010. Dominant control of the South Asian monsoon by  
 403 orographic insulation versus plateau heating. *Nature* 463, 218–222.



404 Burke, K.D., Williams, J.W., Chandler, M.A., Haywood, A.M., Lunt, D.J., Otto-Bliesner,  
 405 B.L., 2018. Pliocene and Eocene provide best analogs for near-future climates.  
 406 *Proceedings of the National Academy of Sciences*, 115, 13288–13293.

407 Cane, M.A., Molnar, P., 2001. Closing of the Indonesian seaway as a precursor to east  
 408 African aridification around 3–4 million years ago. *Nature* 411, 157–162.

409 Cerling, T.E., Harris, J.M., MacFadden, B.J., Leakey, M.G., Quade, J., Eisenmann, V.,  
 410 Ehleringer, J.R., 1997. Global vegetation change through the Miocene/Pliocene  
 411 boundary. *Nature* 389, 153–158.

412 Crampton, J.S., Meyers, S.R., Cooper, R.A., Sadler, P.M., Foote, M., Harte, D., 2018.  
 413 Pacing of Paleozoic macroevolutionary rates by Milankovitch grand cycles.  
 414 *Proceedings of the National Academy of Sciences* 115, 5686–5691.

415 Dianat, M., Darvish, J., Cornette, R., Aliabadian, M., Niolas, V., 2017. Evolutionary  
 416 history of the Persian Jird, *Meriones persicus*, based on genetics, species  
 417 distribution modelling and morphometric data. *Journal of Zoological Systematics &*  
 418 *Evolutionary Research*, 55, 29–45.

419 Ding, Z., Yang, S., Hou, S., Wang, X., Chen, Z., Liu, T., 2001. Magnetostratigraphy and  
 420 sedimentology of the Jingchuan red clay section and correlation of the Tertiary  
 421 eolian red clay sediments of the Chinese Loess Plateau. *Journal of Geophysical*  
 422 *Research: Solid Earth*, 106, 6399–6407.

423 Dowsett, H.J., Chandler, M.A., Cronin, T.M. and Dwyer, G.S. Middle Pliocene sea  
 424 surface temperature variability. *Paleoceanography*, 20, PA2014 (2005).

425 Fedorov, A.V., Dekens, P.S., McCarthy, M., Ravelo, A.C., deMenocal, P.B., Barreiro,  
 426 M., Pacanowski, R.C., Philander, S.G., 2006. The Pliocene Paradox (Mechanisms  
 427 for a Permanent El Nino). *Science* 312, 1485–1489.

428 Hao, Q., Wang, L., Oldfield, F., Peng, S., Qin, L., Song, Y., Xu, B., Qiao, Y.,  
 429 Bloemendal, J., Guo, Z., 2012. Delayed build-up of Arctic ice sheets during  
 430 400,000-year minima in insolation variability. *Nature* 490, 393–396.

431 Haug, G.H., Tiedemann, R., 1998. Effect of the formation of the Isthmus of Panama on  
 432 Atlantic Ocean thermohaline circulation. *Nature* 393, 673–676.

433 Haug, G.H., Tiedemann, R., Zahn, R., Ravelo, A.C., 2001. Role of Panama uplift on  
 434 oceanic freshwater balance. *Geology*, 29, 207–210.

435 Herbert, T.D., Lawrence, K.T., Tzanova, A., Peterson, L.C., Caballero-Gill, R., Kelly,  
 436 C.S., 2016. Late Miocene global cooling and the rise of modern ecosystems. *Nature*  
 437 *Geoscience* 9, 843–847.

438 Hinnov, L.A., 2000. New perspectives on orbitally forced stratigraphy. *Annual Review of*  
 439 *Earth and Planetary Sciences* 28, 419–475.

440 Holbourn, A.E., Kuhnt, W., Clemens, S.C., Kochhann, K.G., Jöhnck, J., Lübbes, J.,  
 441 Andersen, N., 2018. Late Miocene climate cooling and intensification of southeast  
 442 Asian winter monsoon. *Nature Communications* 9, 1584.

443 Huang, Y., Clemens, S.C., Liu, W., Wang, Y., Prell, W.L., 2007. Large-scale  
 444 hydrological change drove the late Miocene C4 plant expansion in the Himalayan  
 445 foreland and Arabian Peninsula. *Geology* 35, 531–534.

446 LaRiviere, J.P., Ravelo, A.C., Crimmins, A., Dekens, P.S., Ford, H.L., Lyle, M., Wara,  
 447 M.W., 2012. Late Miocene decoupling of oceanic warmth and atmospheric carbon  
 448 dioxide forcing. *Nature* 486, 97–100.

449 Laskar, J., Correia, A.C.M., Gastineau, M., Joutel, F., Levrard, B., Robutel, P., 2004.  
 450 Long term evolution and chaotic diffusion of the insolation quantities of Mars.  
 451 *Icarus*, 170, 343–364.

452 Laskar, J., Joutel, F., Boudin, F., 1993. Orbital, precessional, and insolation quantities for  
 453 the Earth from -20 Myr to +10 Myr. *Astronomy and Astrophysics*, 270, 522–533.

454 Lawrence, K.T., Liu, Z., Herbert, T.D., 2006. Evolution of the Eastern Tropical Pacific  
 455 Through Plio-Pleistocene Glaciation. *Science* 312, 79–83.

456 Lewis, A.R., Marchant, D.R., Ashworth, A.C., Hedenäs, L., Hemming, S.R., Johnson,  
 457 J.V., Leng, M.J., Machlus, M.L., Newton, A.E., Raine, J.I., Willenbring, J.K., 2008.  
 458 Mid-Miocene cooling and the extinction of tundra in continental Antarctica.  
 459 *Proceedings of the National Academy of Sciences* 105, 10676–10680.

460 Li, F., Rousseau, D.D., Wu, N., Hao, Q., Pei, Y., 2008. Late Neogene evolution of the  
 461 East Asian monsoon revealed by terrestrial mollusk record in Western Chinese  
 462 Loess Plateau: from winter to summer dominated sub-regime. *Earth Planet. Sci.*  
 463 *Lett.* 274, 439–447.

464 Liu, J., Tian, J., Liu, Z., Herbert, T.D., Fedorov, A.V., Lyle, M., 2019. Eastern equatorial  
 465 Pacific cold tongue evolution since the late Miocene linked to extratropical climate.  
 466 *Science advances* 5, eaau6060.

467 Molnar, P., 2008. Closing of the Central American Seaway and the Ice Age: A critical  
 468 review. *Paleoceanography*, 23, PA2201, doi: 10.1029/2007PA001574.

469 Naish, T., Powell, R., Levy, R., Wilson, G., Scherer, R., Talarico, F., Krissek, L.,  
 470 Niessen, F., Pompilio, M., Wilson, T., Carter, L., 2009. Obliquity-paced Pliocene  
 471 West Antarctic ice sheet oscillations. *Nature* 458, 322–329.

472 Nie, J., King, J.W., Fang, X., 2008. Tibetan uplift intensified the 400 ky signal in  
 473 paleoclimate records at 4 Ma. *Geological Society of America Bulletin* 120, 1338–  
 474 1344.

475 Nie, J. 2018. The Plio-Pleistocene 405-kyr climate cycles. *Palaeogeography*,  
 476 *palaeoclimatology, palaeoecology* 510, 26–30.

477 Ogg, J. G., 2012. Geomagnetic Polarity Time Scale. In F. M. Gradstein, J. G. Ogg, M. D.  
 478 Schmitz, & G. M. Ogg (Eds.), *The Geologic Time Scale 2012*. Amsterdam: Elsevier,  
 479 (pp. 85–113).

480 Prell, W.L., Kutzbach, J.E, 1992. Sensitivity of the Indian monsoon to forcing  
 481 parameters and implications for its evolution. *Nature* 360, 647–652.

482 Ravelo, A.C., Andreasen, D.H., Lyle, M., Lyle, A.O., Wara, M.W., 2004. Regional  
 483 climate shifts caused by gradual global cooling in the Pliocene epoch. *Nature* 429,  
 484 263–267.

485 Schuster, M., Düringer, P., Ghienne, J.F., Vignaud, P., Mackaye, H.T., Likius, A., 2006.  
 486 Brunet, M. The age of the Sahara Desert. *Science* 311, 821.

487 Sun, J., Zhang, Z., Zhang, L., 2009. New evidence on the age of the Taklimakan Desert.  
 488 *Geology* 37, 159–162.

489 Sun, Y., Yin, Q., Crucifix, M., Clemens, S.C., Araya-Melo, P., Liu, W., Qiang, X., Liu,  
 490 Q., Zhao, H., Liang, L., Chen, H., 2019. Diverse manifestations of the mid-  
 491 Pleistocene climate transition. *Nature communications*, 10, 352.

492 Thiede, J., Winkler, A., Wolf-Welling, T., Eldholm, O., Myhre, A.M., Baumann, K.H.,  
 493 Henrich, R., Stein, R., 1998. Late Cenozoic history of the Polar North Atlantic:  
 494 results from ocean drilling. *Quaternary Science Reviews*, 17, 185–208.

495 van Dam, J., Abdul Aziz, H., Alvarez Sierra, M.A., Hilgen, F.J., van den Hoek Ostende  
 496 L.W., Lourens, L.J., Mein, P., van der Meulen, A.J., Pelaez-Campomanes, P. , 2006.  
 497 Long-period astronomical forcing of mammal turnover. *Nature* 443, 687–691.

498 Westerhold, T., Marwan, N., Drury, A.J., Liebrand, D., Agnini, C., Anagnostou, E.,  
 499 Barnet, J.S., Bohaty, S.M., De Vleeschouwer, D., Florindo, F., Frederichs, T., 2020.  
 500 An astronomically dated record of Earth’s climate and its predictability over the last  
 501 66 million years. *Science*, 369, 1383–1387.

502 Wolf-Welling, T.C., Cremer, M., O’Connell, S., Winkler, A., Thiede, J., 1996. Cenozoic  
 503 Arctic gateway paleoclimate variability: Indications from changes in coarse-fraction  
 504 composition. *Proceedings of the Ocean Drilling Program, Scientific Results* 151,  
 505 515–568.

506 Xu, Y., Yue, L., Li, J., Sun, L., Sun, B., Zhang, J., Ma, J., Wang, J., 2009. An 11-Ma-old  
 507 red clay sequence on the Eastern Chinese Loess Plateau. *Palaeogeography*,  
 508 *Palaeoclimatology, Palaeoecology* 284, 383–391.

509 Xu, Y., Yue, L., Li, J., Wang, J., Sun, B., Sun, L., Zhang, J., Ma, J., 2013. Late Neogene  
 510 red clay in the Fuxing area of western foothills of the Luliang Mountain. *Journal of*  
 511 *Stratigraphy*, 37, 33–40 (in Chinese).

512 Yan, X., Ho, C., Zheng, Q. and Klemas, V., 1992. Temperature and size variabilities of  
 513 the west Pacific warm pool. *Science* 258, 1643–1645.

514 Zachos, J., Pagani, M., Sloan, L., Thomas, E., Billups, K., 2001. Trends, rhythms, and  
 515 aberrations in global climate 65 Ma to present. *science* 292, 686–693.

516 Zheng, S., Zhang, Z., 2000. Late Miocene-Early Pleistocene micromammals from  
 517 Wenwanggou of Lingtai, Gansu, China. *Vertebrata Palasiatica*, 38, 58–71.

518 Zheng, S., Zhang, Z., 2001. Late Micene-early Pleistocene biogeography of the Leijiahe  
 519 area, Lingtai, Gansu. *Vertebrata Palasiatica* 39, 215–228 (in Chinese).

520 Zhang, R., Kravchinsky, V. A., Anwar, T., Yue, L., Li, J., Jiao, J., 2018. Comment on  
 521 "Late Miocene-Pliocene Asian monsoon intensification linked to Antarctic ice-sheet  
 522 growth" [*Earth Planet. Sci. Lett.* 444 (2016) 75-87]. *Earth and Planetary Science*  
 523 *Letters* 503, 248–251.

524 Zhang, R., Kravchinsky, V. A., Qin, J., Goguitchaichvili, A., Li, J., 2021. One and a Half  
 525 Million Yearlong Aridity During the Middle Eocene in North-West China Linked to

526 a Global Cooling Episode. *Journal of Geophysical Research: Solid Earth* 126,  
527 e2020JB021037.

528 Zhang, R., Wei, X., Kravchinsky, V. A., Yue, L., Zheng, Y., Qin, J., Yang, L., Ma, M.,  
529 Xian, F., Gong, H., Zhang, Y., Liu, X., 2021. “Tiny wiggles” in the late Miocene  
530 red clay deposits in the north-east of the Tibetan Plateau. *Geophysical Research*  
531 *Letters*, 48, e2021GL093962.

532 Zhang, R., Li, X., Xu, Y., Li, J., Sun, L., Yue, L., Pan, F., Xian, F., Wei, X., Cao, Y.,  
533 2022. The 173-kyr obliquity cycle pacing the Asian monsoon in the eastern Chinese  
534 Loess Plateau from late Miocene to Pliocene. *Geophysical Research Letters*, 49,  
535 e2021GL097008.

536

## Figure Captions

**Figure 1.** (a) Topographic map of the present-day Chinese Loess Plateau with studied locations (yellow star and yellow dots). Liulin (yellow star); SL- Shilou, JC- Jingchuan. (b) Map showing the location of LL (green triangle) and SL (red star) red clay sections and the surrounding main rivers. Red dashed lines represent the contours and the elevation is in meters.

**Figure 2.**  $\chi$ -T curves for selected samples from the Liulin red clay sequence. The red and blue lines represent heating and cooling curves, respectively.

**Figure 3.** Representative thermal demagnetization curves for different depths.

**Figure 4.** Lithostratigraphy, inclination, declination and VGP as a function of depth, and the magnetic polarity interpretation of the Liulin red clay section, together with a correlation to the geomagnetic timescale (Ogg, 2012). Red dots show the measuring samples. Legend: 1—red clay with strong pedogenesis, 2—sandy red clay, 3—red clay with weak pedogenesis, 4—carbonate layer, 5—mudstone, 6—fossil, 7—sandstone, 8—gravel, 9—carbonate nodules.

**Figure 5.** Wavelet analysis of the magnetic susceptibility signal before (a) and after



tuning (b), the coarse fraction ( $>63\mu\text{m}$ ) content before (c) and after tuning (d). Magnetic susceptibility and Grain size was detrended with the Lowess smoothing method. The red line is the two-band-filter signal with bandwidths of 350–500 kyr and 80–125 kyr. The green solid line shows the long trend of MS (a,b) and GS (c,d) signals. The purple dashed line marks the orbital period. The thin black contour encloses regions of greater than 95% confidence for a red-noise process with a lag coefficient of 0.8. The thick black contour indicates the cone of influence. The global wavelet spectrum to the right illustrates the mean red noise spectrum, as indicated by the green dashed line. The color bars correspond to wavelet power.

**Figure 6.** Sedimentation rates are determined on the basis of the magnetostratigraphic correlations. Black dashed lines denote the typical sedimentation rate range for the red clay of the CLP (Zhang et al., 2018). The red dashed line represents the average sedimentation rate of the Liulin section determined by the magnetostratigraphy.

**Figure 7.** Comparison of magnetic susceptibility as a function of age from red clay sections in the Chinese Loess Plateau. Three stages of different climate conditions as shown by the MS. (a) MS of the LL red clay section. (b) MS of the SL red clay section (Anwar et al., 2015). (c) LMS of the combined LL and SL red clay sections. (d) MS of the JC red clay section (Ding et al., 2001). (e) Wavelet analysis of magnetic susceptibility records from the LMS. (f) Wavelet spectrum of magnetic susceptibility from the JC section.

579

580 **Figure 8.** Milankovitch cycles between 7.8 and 2.5 Ma derived from the astronomical  
581 solution (Laskar et al., 2004) and the Asian monsoon record. a. Amplitude modulation of  
582 the precession solution (blue line) with its envelope curve (black dashed line) with the  
583 ~100,000 and ~405,000 cycles. b. Amplitude modulation (green line) of the obliquity  
584 solution (Laskar et al., 2004) (blue line). c. Eccentricity solution. d. Long magnetic  
585 susceptibility (LMS) detrended by the Lowess smoothing method (blue). f. Magnetic  
586 susceptibility from JC section after detrending using the Lowess smoothing method (blue)  
587 (Ding et al., 2001). Red lines indicate the two-band filter with bandwidths of 350–500  
588 kyr and 80–125 kyr in d,e,f,g,h. Green dashed curves show the ~1.2 Myr obliquity  
589 modulations coupling with MS results (d,e).

590

591 **Fig. 9.** Compilation of Asian monsoon and global climatic proxies. a. Illustration of the  
592 eccentricity solution (Laskar et al., 2004) (blue solid and dashed lines) and the ~1.2 Myr  
593 grand cycles/obliquity modulations (green dashed line). b. Combined LMS record of the  
594 LL and SL sections. c. MS from JC section in the central CLP (Ding et al., 2001). d.  
595 Benthic  $\delta^{18}\text{O}$  global record (Westerhold et al., 2020) (blue) and benthic  $\delta^{18}\text{O}$  record  
596 from ODP Site 1148 (Tian et al., 2008) (orange). e. Stacked SST from mid-high (pink)  
597 and tropical (brown) latitudes. Pacific mid-high latitude records are integrated from  
598 DSDP Site 594, ODP Sites 883/884, 887, 1010, 1012, 1021, 1125 and 1208; Pacific  
599 tropical records are integrated from the IODP Sites U1337, U1338, ODP Sites 846, 847,  
600 850 and 1241 (Liu et al., 2019). f. Atmospheric  $\text{CO}_2$  history during the past 8 Myr from

different proxies (Beerling et al., 2011; Herbert et al., 2016). Horizontal red line indicates the Northern Hemisphere glaciation threshold (approx. 280 ppm). g.  $\delta^{13}\text{C}$  record (yellow) and carbonate sand-fraction mass accumulation rates (purple) from ODP site 999 (Haug et al., 1998).

**Fig. 10.** The simplified climate mode for Asian monsoon from late Miocene to Pliocene. a. Eccentricity solution (Laskar et al., 2004) (blue solid and dashed lines), obliquity solution (Laskar et al., 2004) (red line), and the ~1.2 Myr grand cycles (green solid line from 8 to 4 Ma and green dashed line from 4 to 2.5 Ma). b. Mathematical model showing the 1.2 Myr grand cycles (red) during the 8 to 4 Ma ( $Y1 = \cos(2 \times \pi \times (1/1200) \times t)$ ); the 400 eccentricity cycles (blue) ( $Y2 = \sin(2 \times \pi \times (1/400) \times t)$ ) and the stepped tectonics (green arrow) ( $Y3$ ) during the 4 to 2.5 Ma; compound of long eccentricity and stepped tectonics (yellow) ( $Y4 = Y2 \times Y3$ ).

Figure 1.

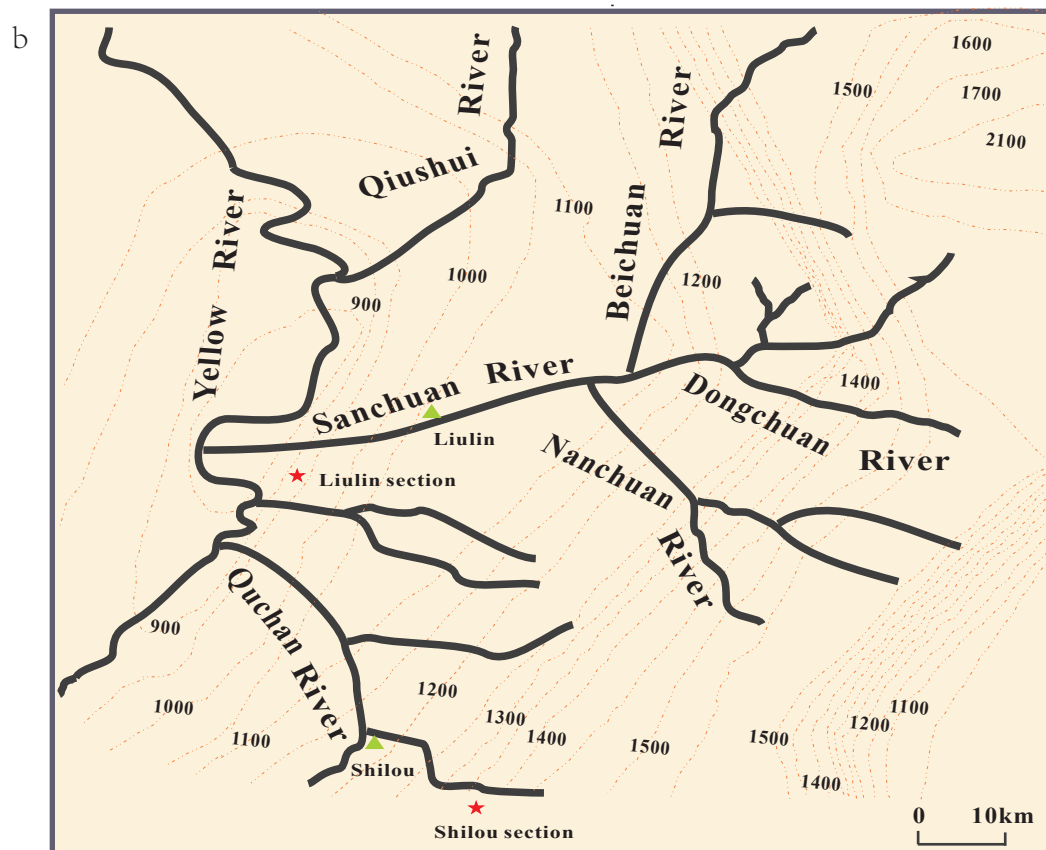
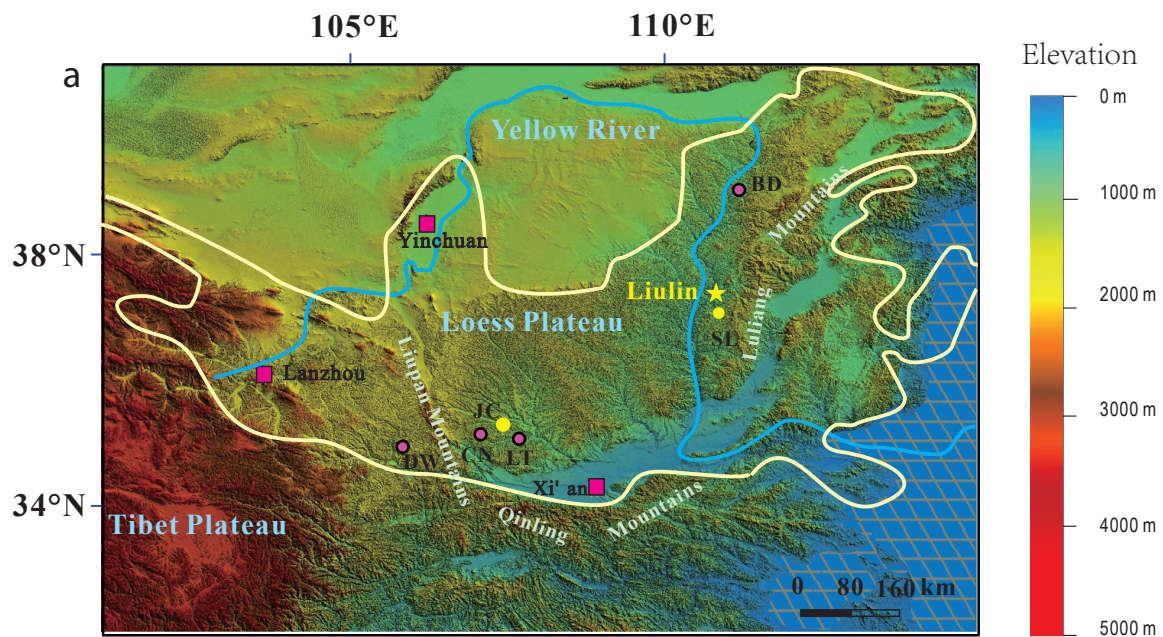


Figure 2.

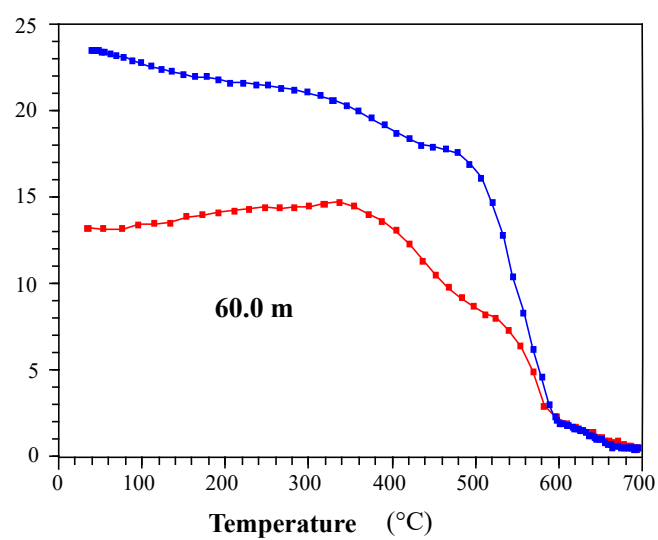
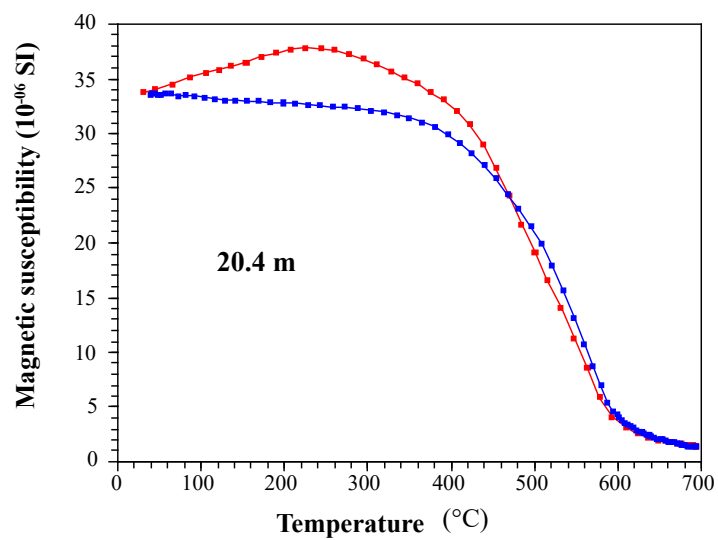
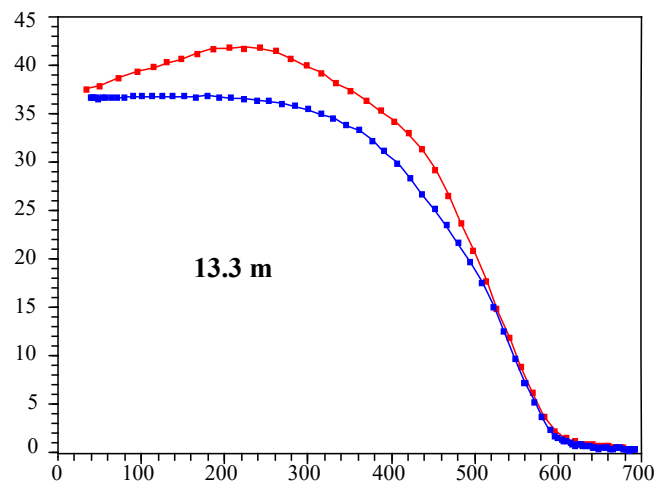
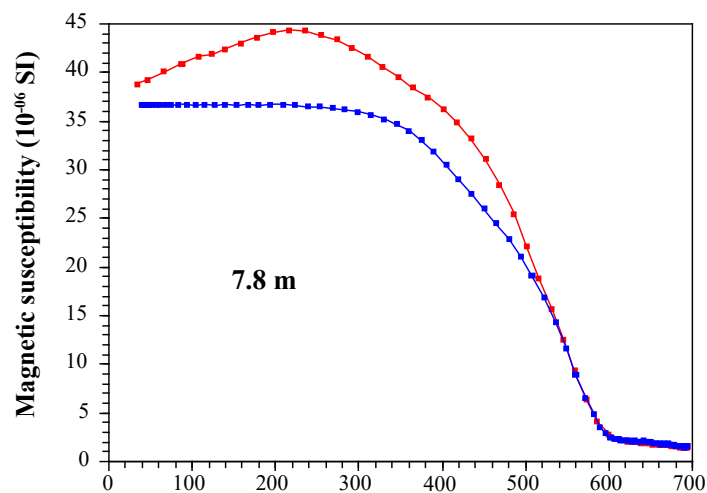


Figure 3.



—● horizontal compenant  
—○ vertical compenant

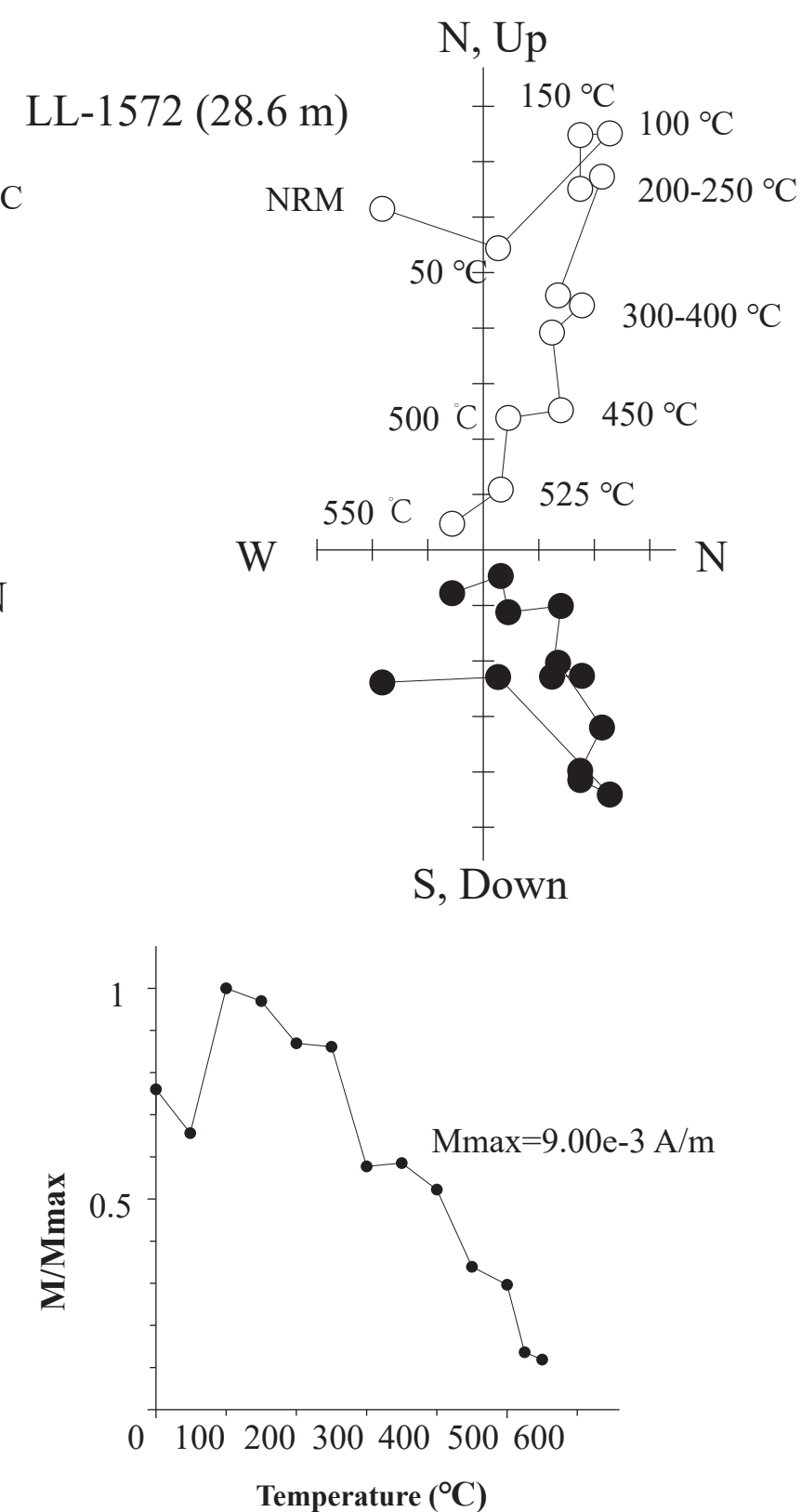
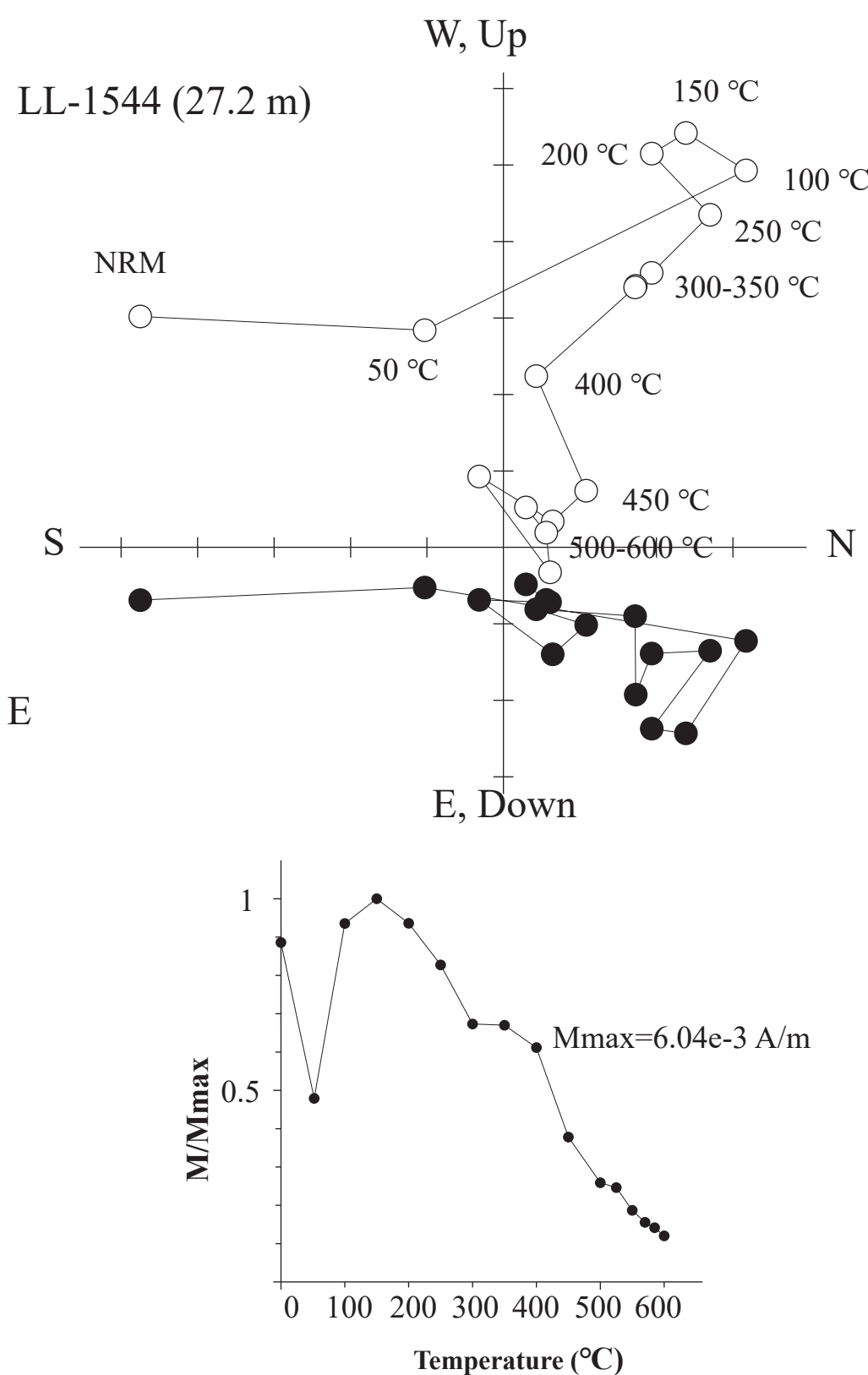
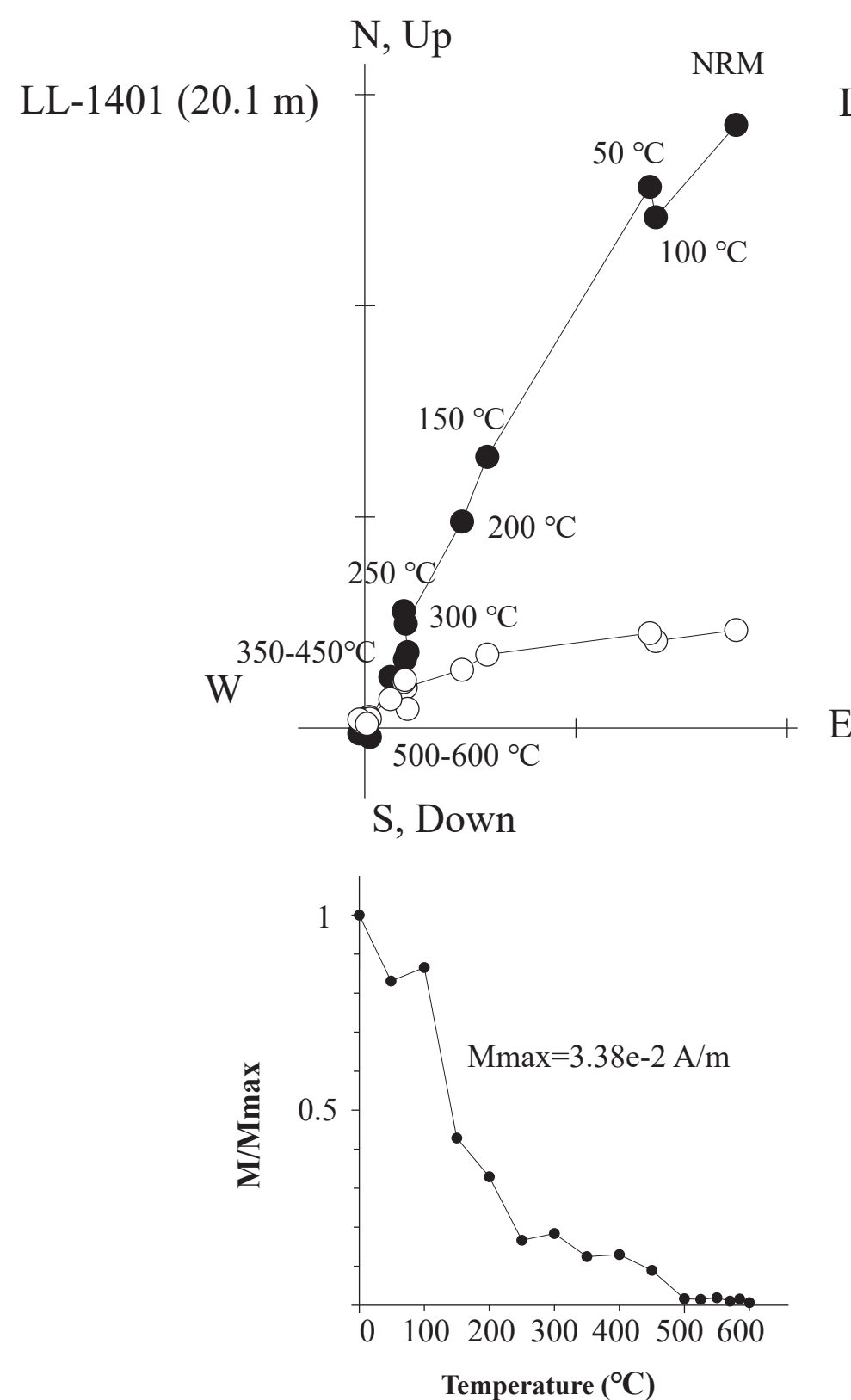
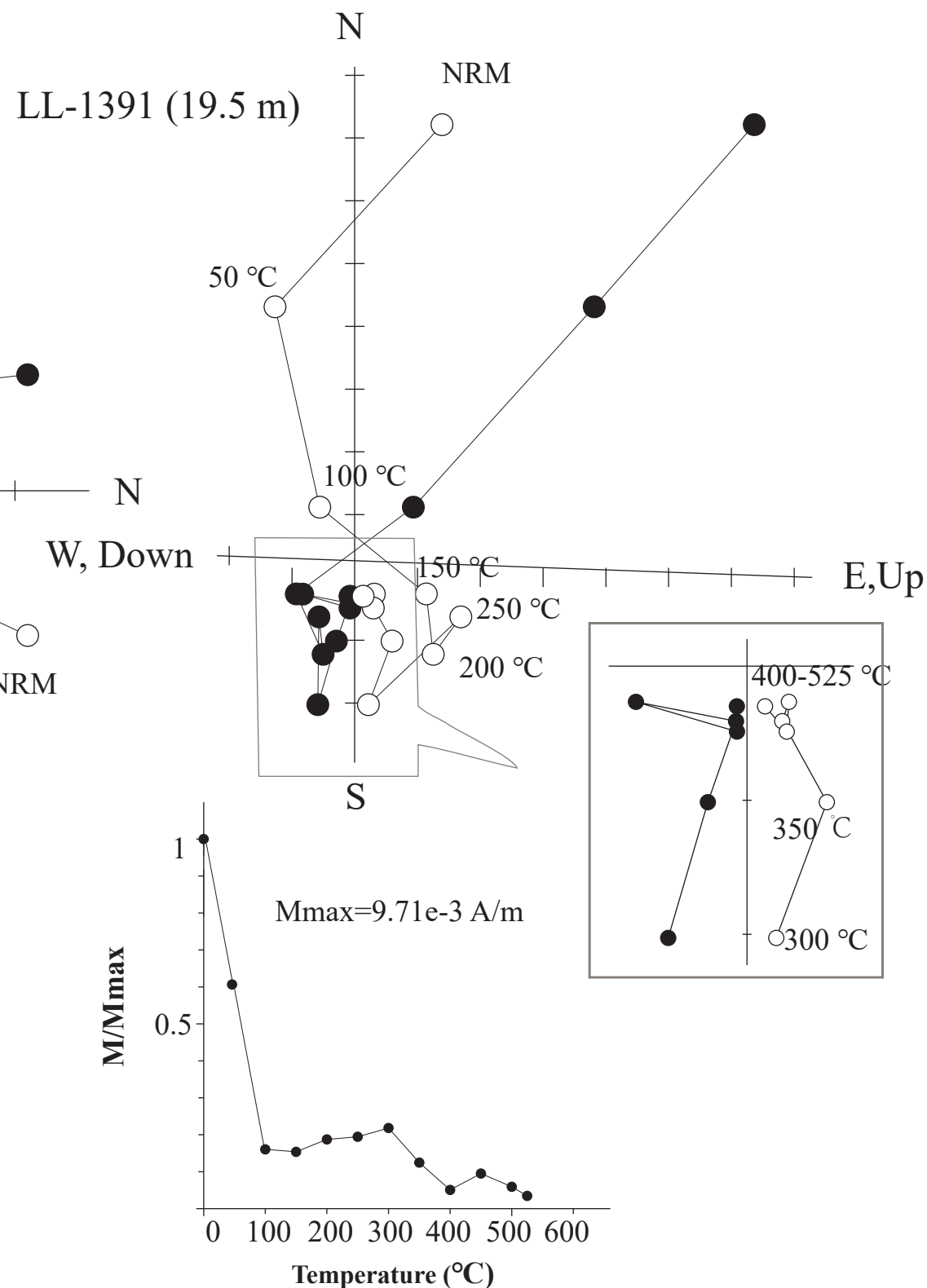
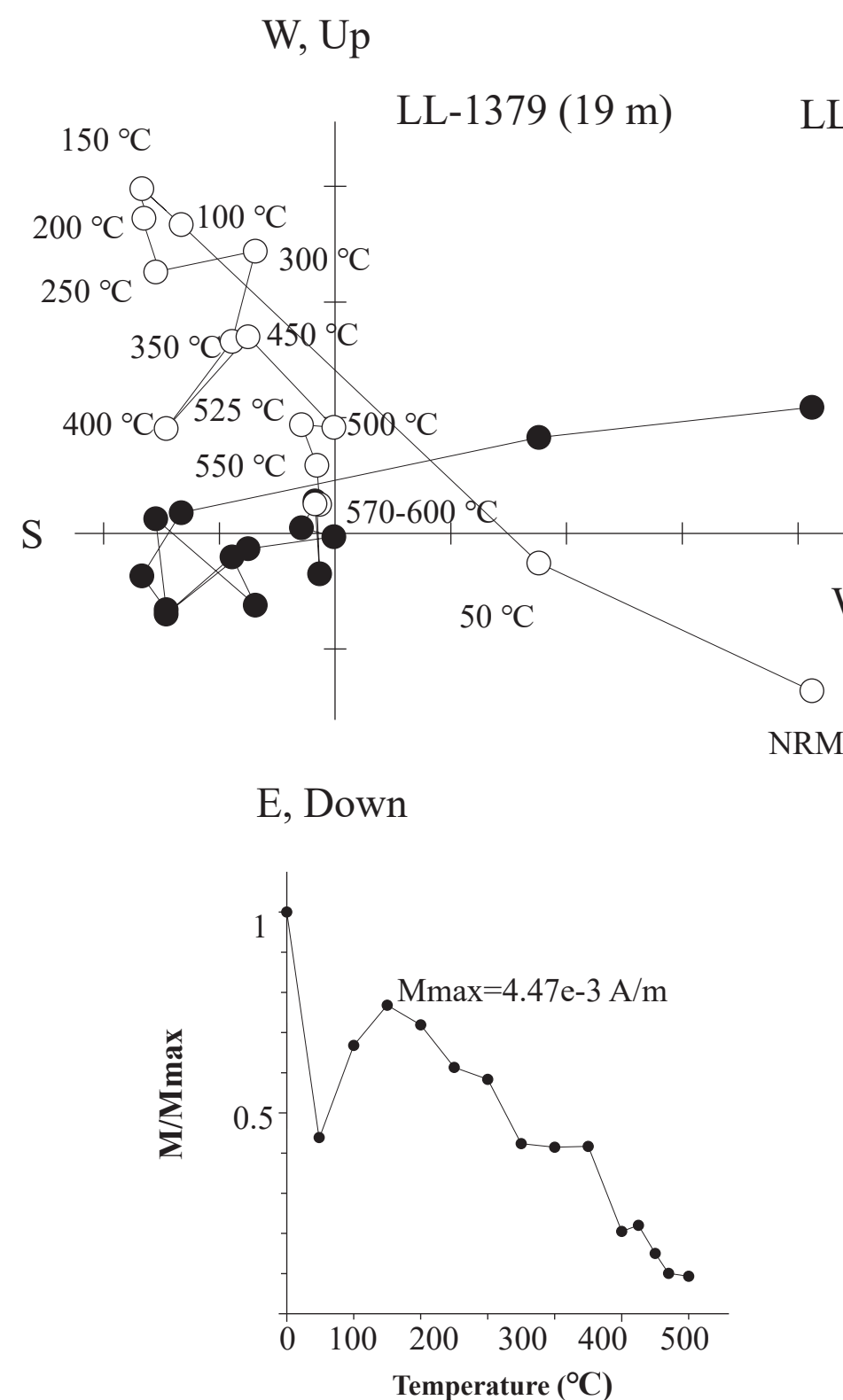
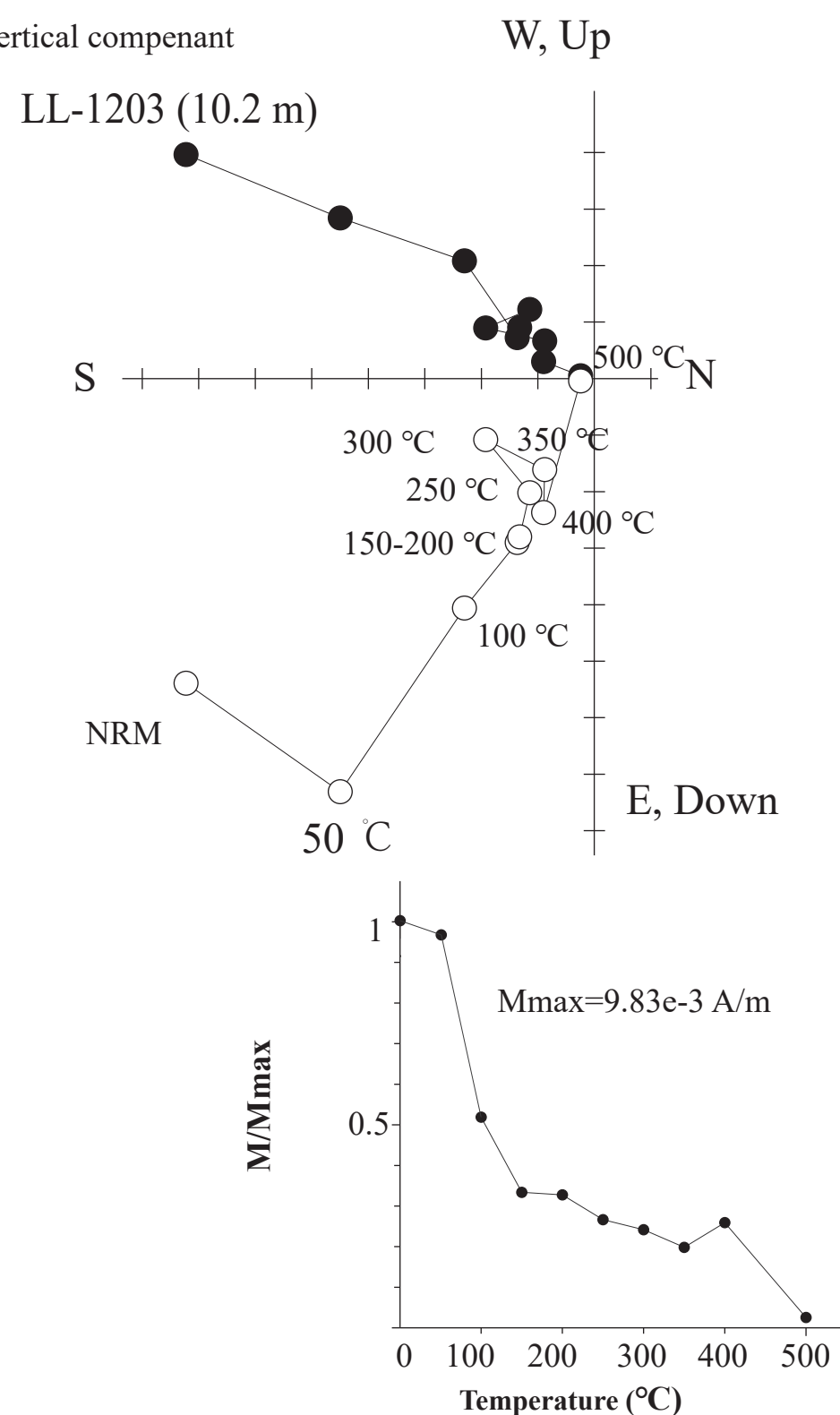


Figure 4.

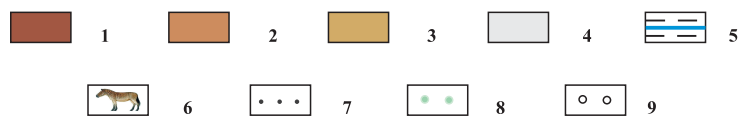
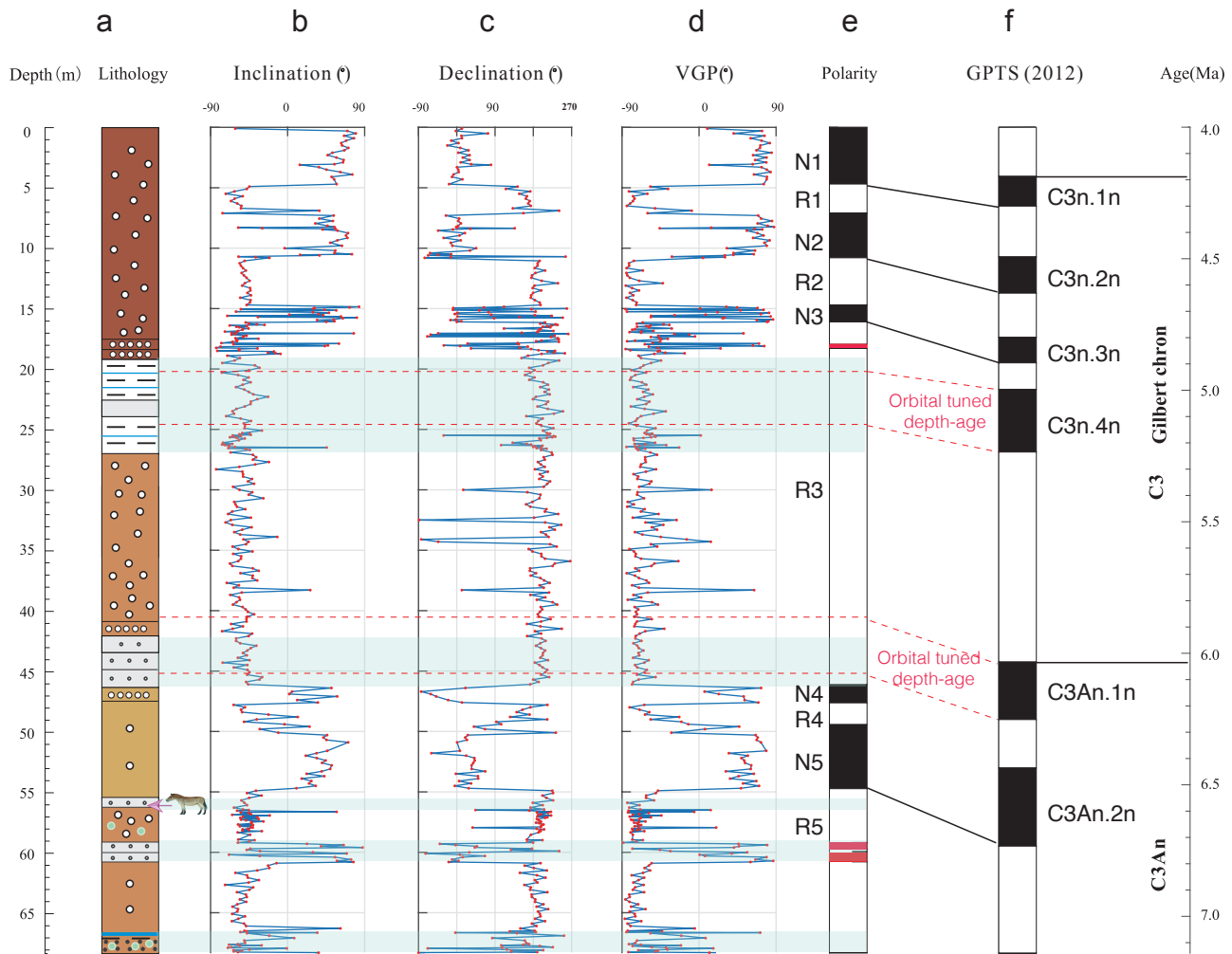


Figure 5.

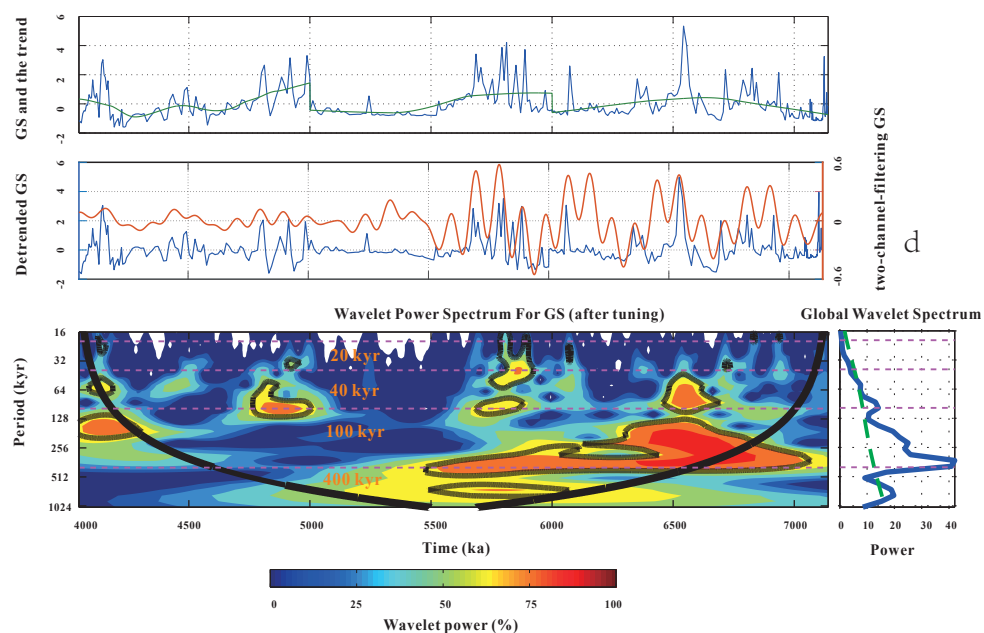
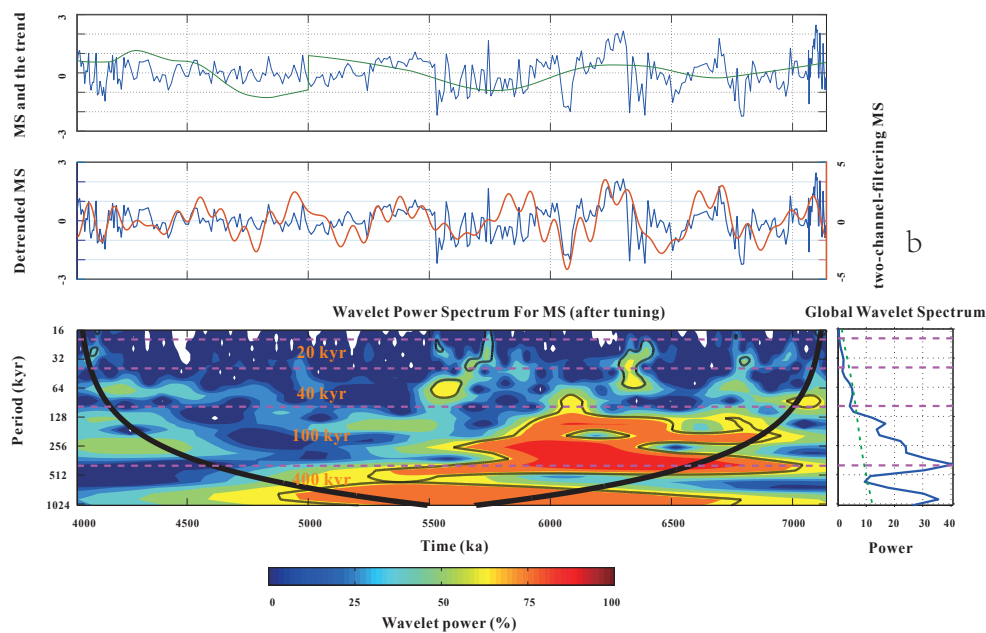
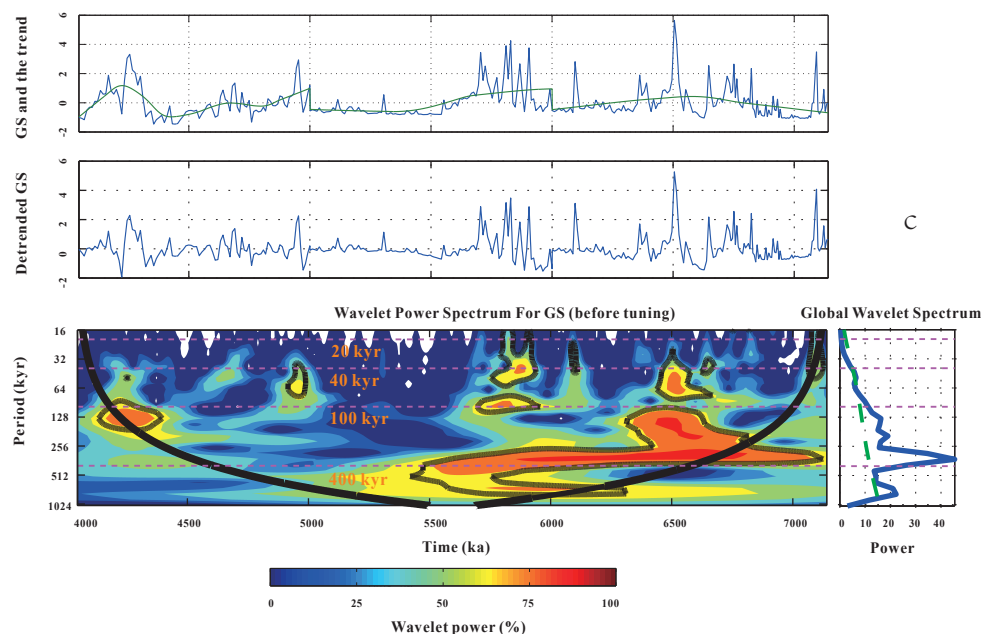
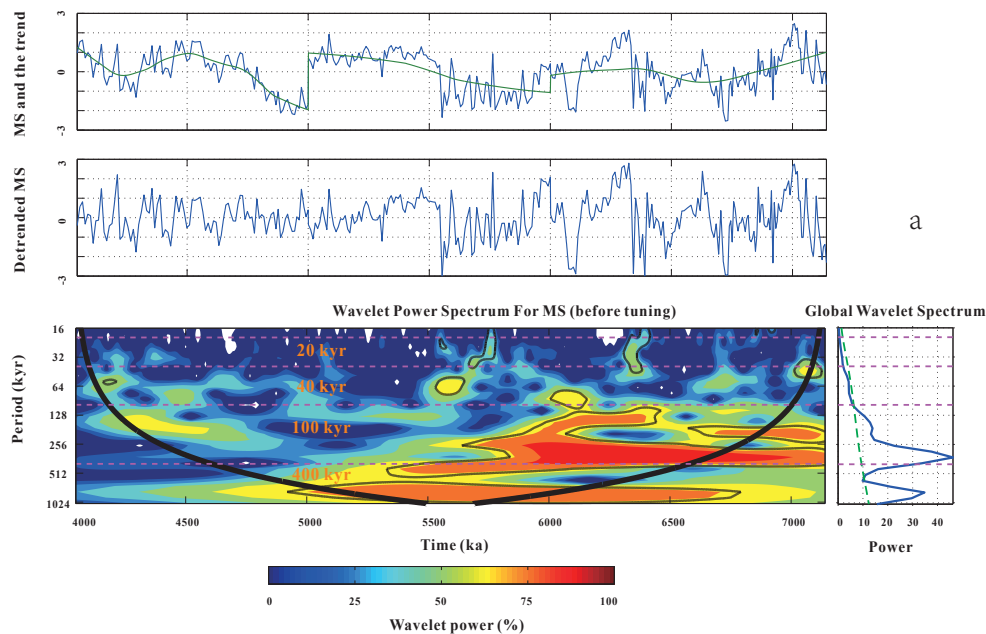
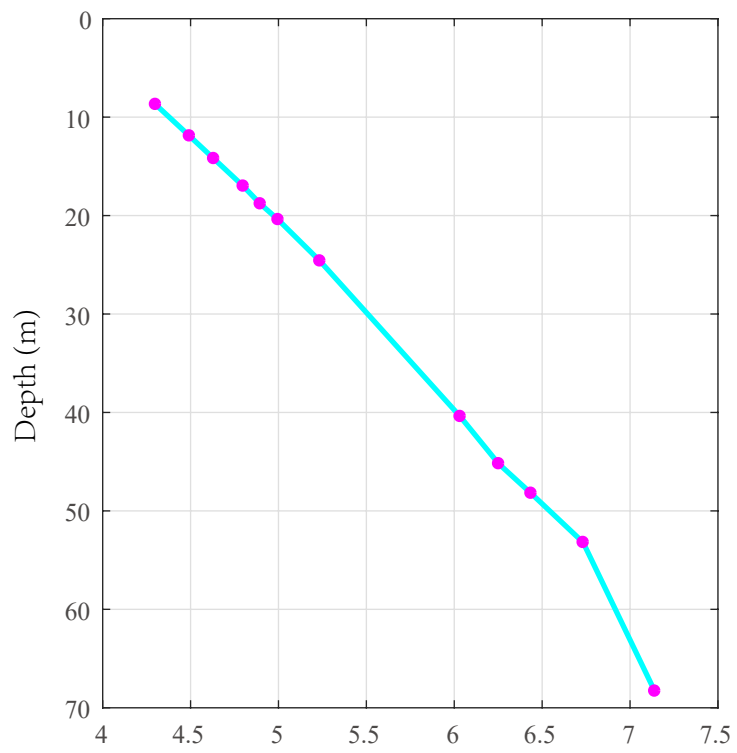


Figure 6.

Age (Ma)



Age (Ma)

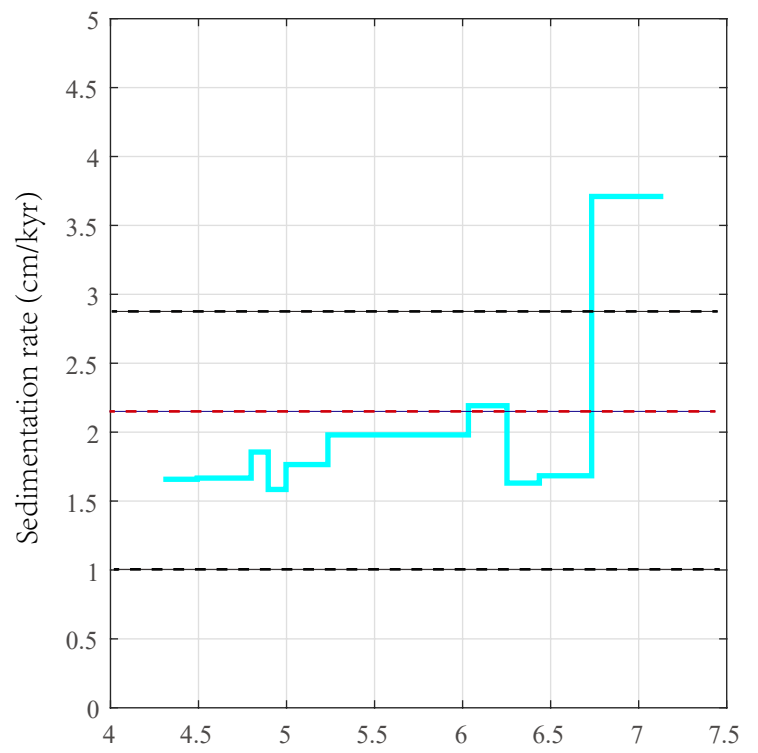


Figure 7.



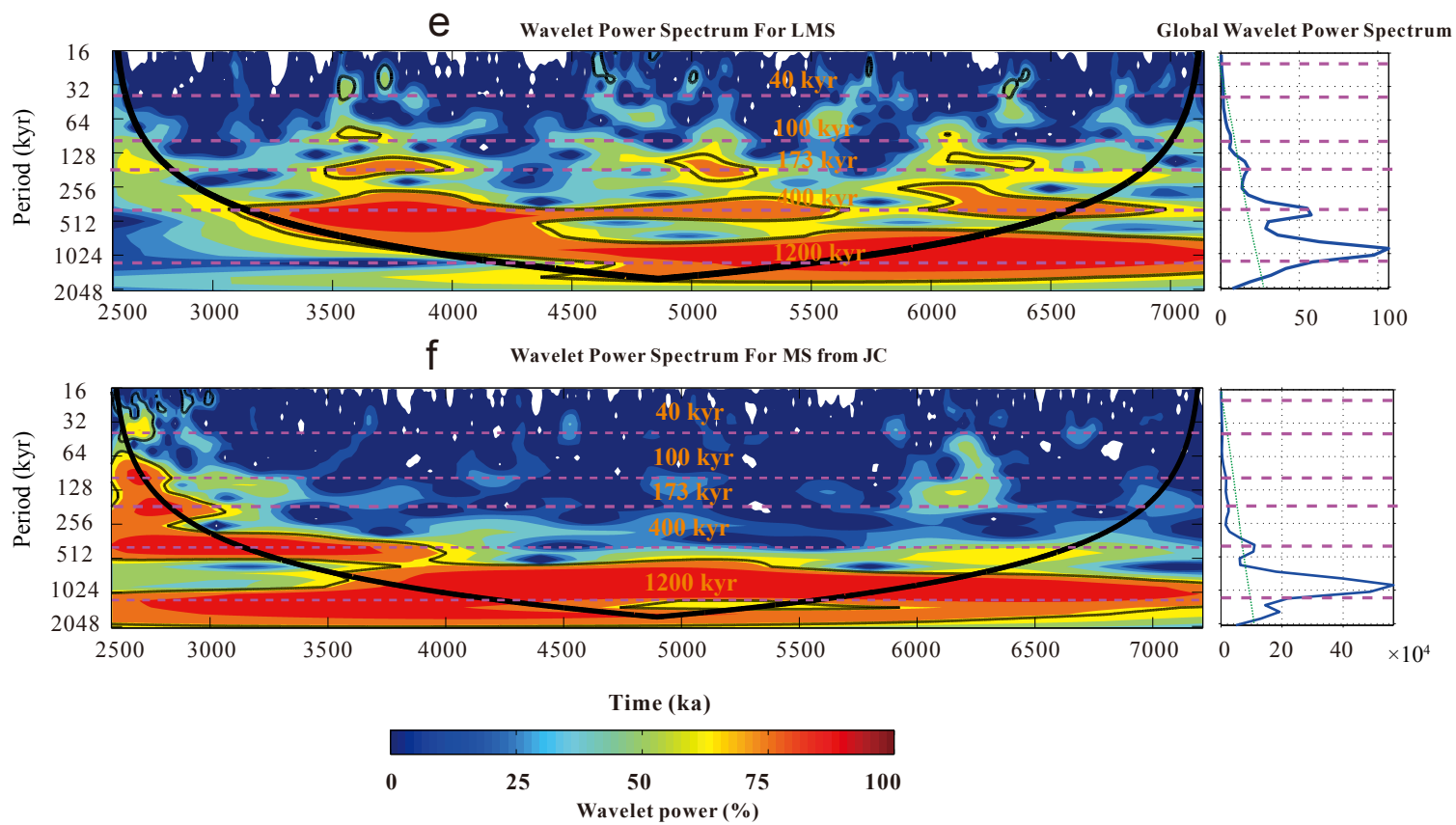
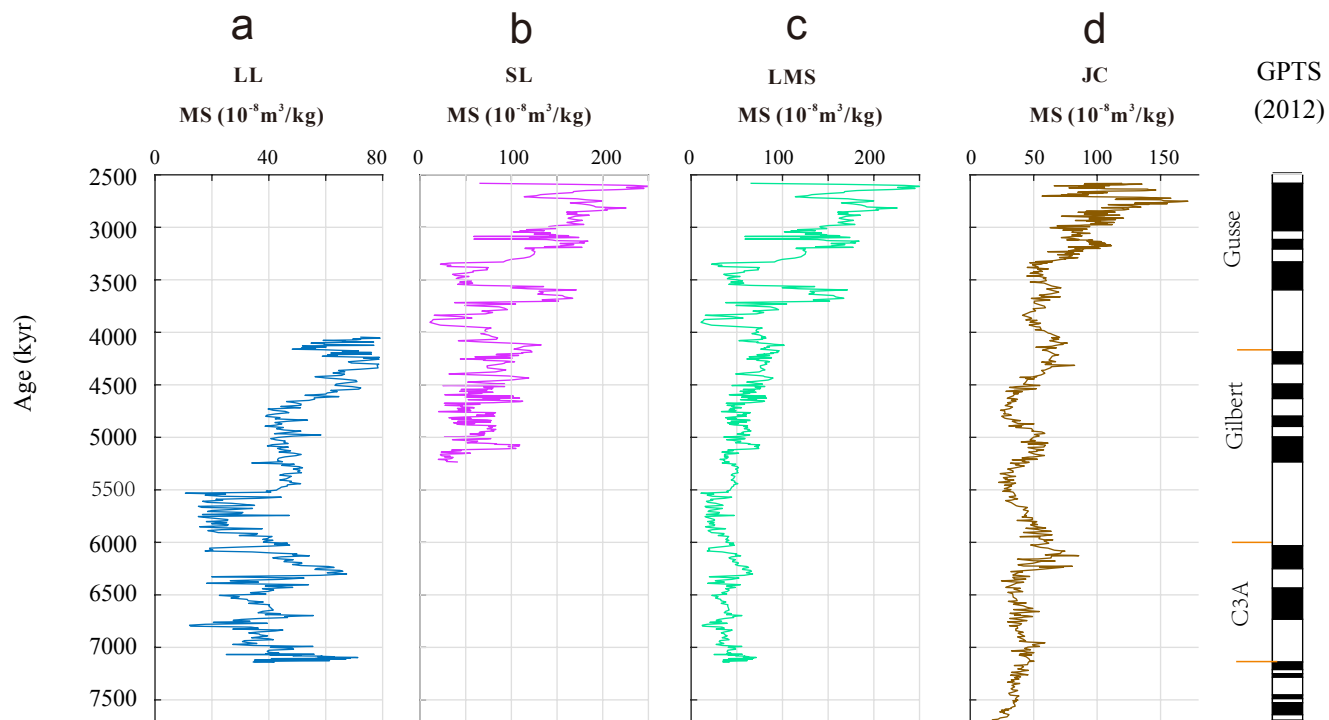


Figure 8.

3000 3500 4000 4500 5000 5500 6000 6500 7000 7500

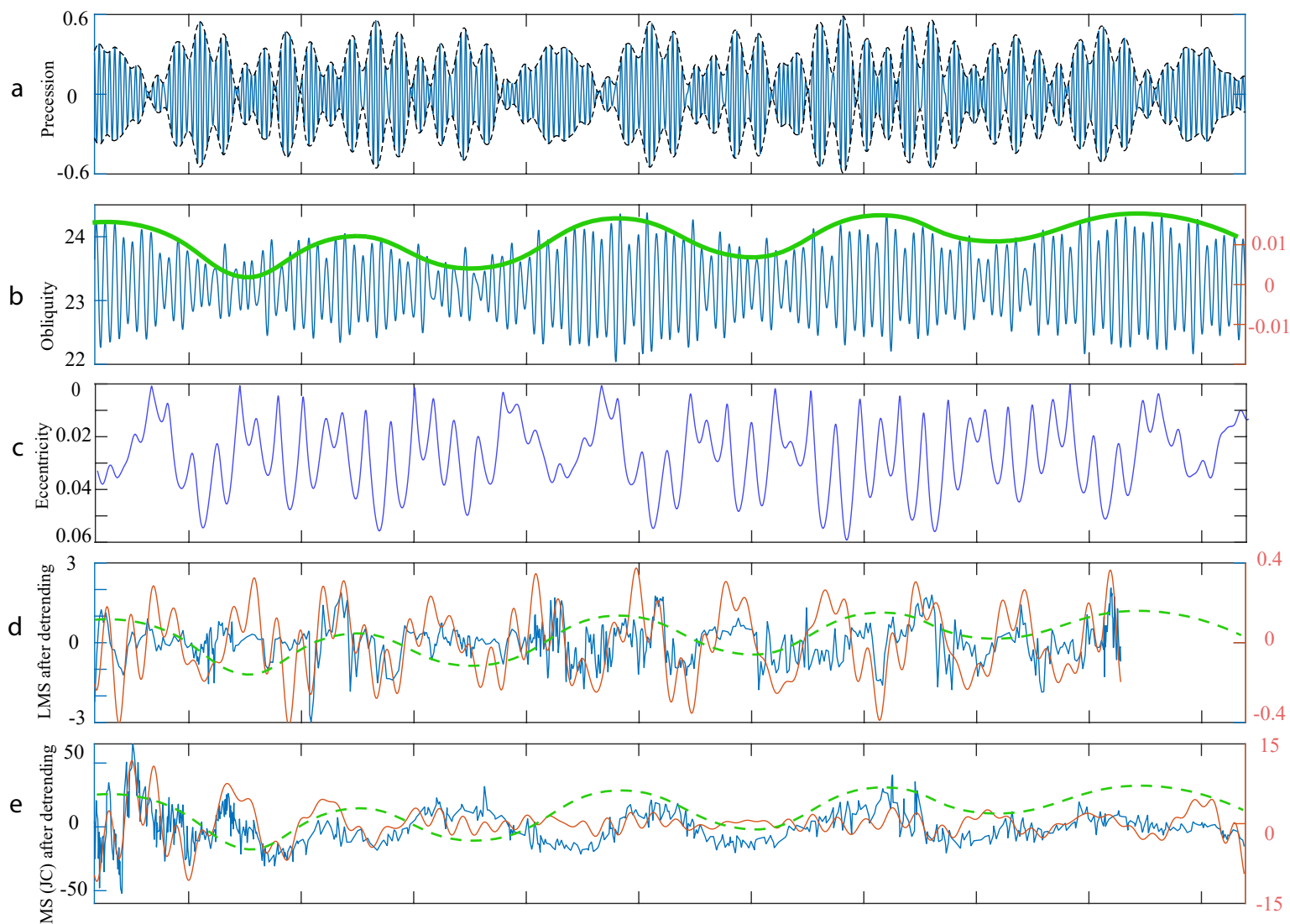


Figure 9.

405-kyr eccentricity cycle  
dominant Asian monsoon

1.2-Myr obliquity modulation dominant Asian monsoon

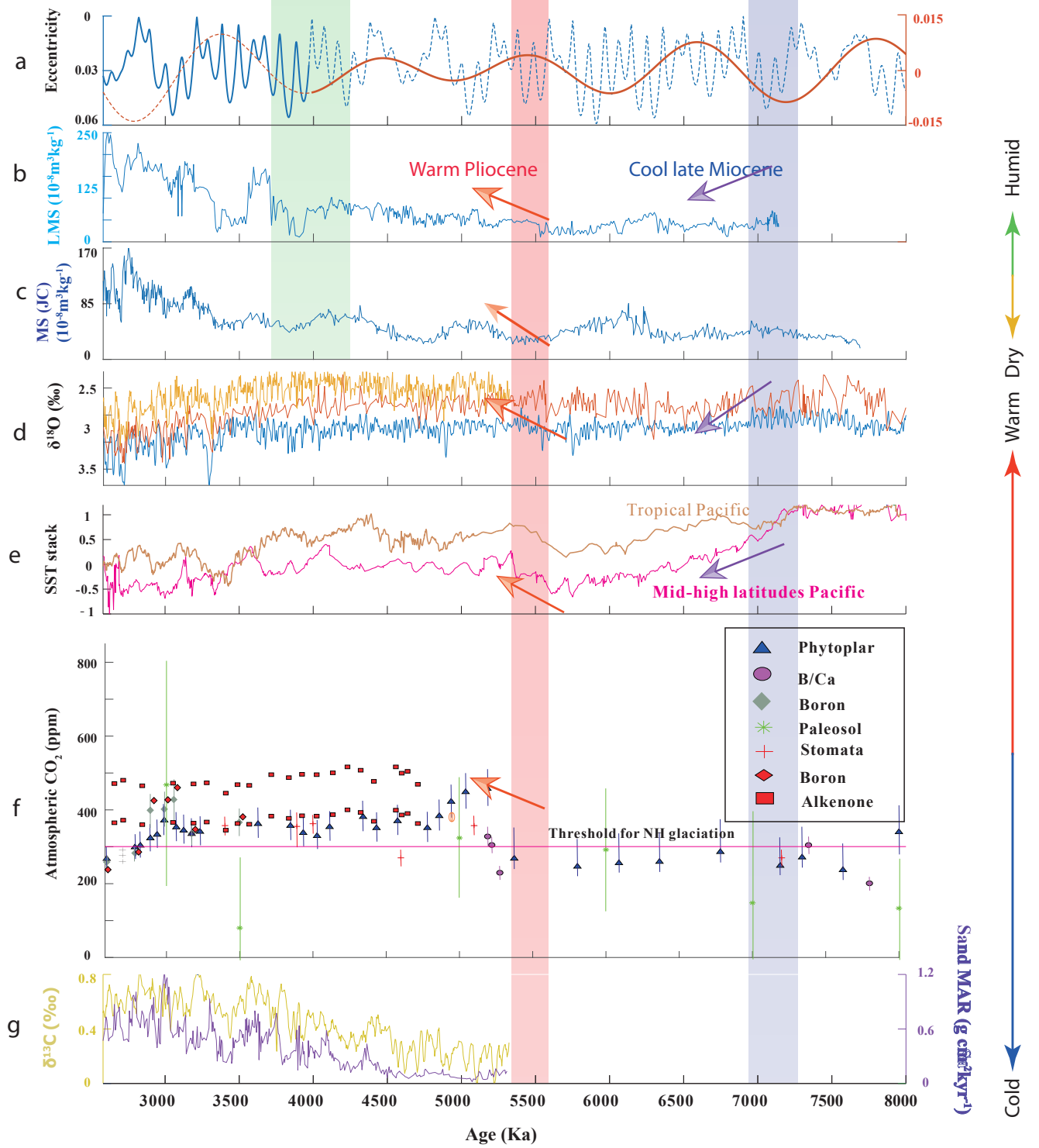
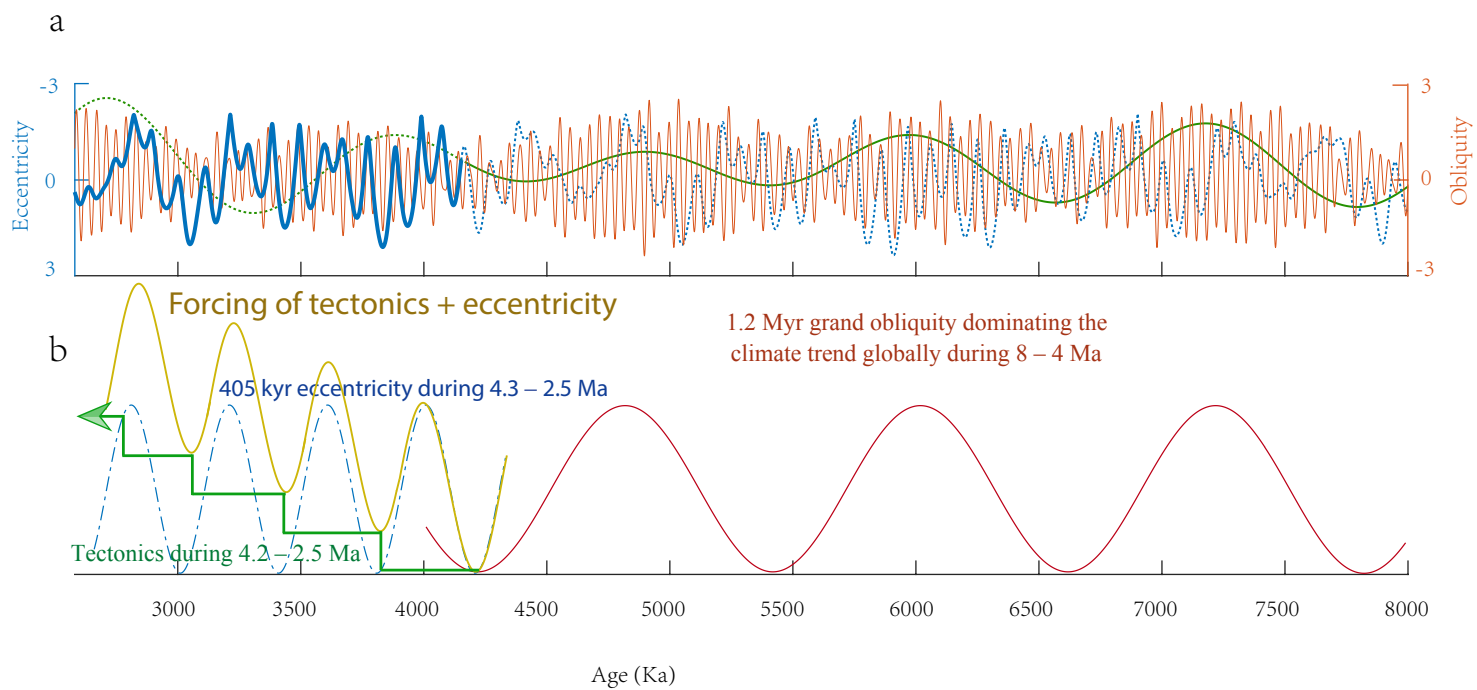


Figure 10.



## Supplementary Material

for the manuscript

### 1.2-million-year band of Earth–Mars obliquity modulation on the evolution of cold late Miocene to warm early Pliocene climate

Jie Qin<sup>1,2</sup>, Rui Zhang<sup>1,2\*</sup>, Vadim A. Kravchinsky<sup>1,2,\*</sup>, Jean-Pierre Valet<sup>1,3</sup>, Leonardo Sagnotti<sup>4</sup>,  
Jianxing Li<sup>5</sup>, Yong Xu<sup>6</sup>, Taslima Anwar<sup>1,2</sup>, Leping Yue<sup>1</sup>

<sup>1</sup> Institute of Cenozoic Geology and Environment, State Key Laboratory of Continental Dynamics, Department of Geology, Northwest University, 710069 Xi'an, China

<sup>2</sup> Geophysics, Department of Physics, University of Alberta, T6G2E1 Edmonton, Canada

<sup>3</sup> Institut de Physique du Globe de Paris, 75238 Paris cedex 05, France

<sup>4</sup> Istituto Nazionale di Geofisica e Vulcanologia, 00143 Roma, Italy

<sup>5</sup> Chengdu Center of Geological Survey, Geological Survey of China, 610081 Chengdu, China

<sup>6</sup> Xi'an Center of Geological Survey, China Geological Survey, 710054 Xi'an, China

\* Corresponding author emails: [ruizhang@nwu.edu.cn](mailto:ruizhang@nwu.edu.cn); [vadim@ualberta.ca](mailto:vadim@ualberta.ca)

This PDF file includes:

Supplementary Material Text S1– S3

Supplementary Material Figs. 1–3

References



## **S1 - Introduction**

The East Asian monsoon (EAM) system controls precipitation and dust accumulation by seasonal alternation of inputs of warm moist air from Indian Ocean and Pacific Ocean, and dry dust-bearing winds from the high latitudes and high altitudes, which resulted in the creation of the typical sedimentary sequence of the Chinese Loess Plateau (CLP). Heller and Liu (1982) built the robust chronology for the 2.5 Ma loess deposits. The age of underlain eolian red clay was first assigned to the Pliocene at 4 – 5 Ma (Evans et al., 1991; Zheng et al., 1992) and later to the late Miocene at ~7 – 8 Ma (Ding et al., 1998, Sun et al., 1998a, b), the early Miocene at 22 Ma (Guo et al., 2002) and the late Oligocene at 25 Ma (Qiang et al., 2011). Recent magnetostratigraphic studies, however, raised a problem of inconsistency in the reconstructed chronology for the eolian red clay sections in the eastern CLP. For example, a debate exists about the dating of the Jiaxian section where Ding et al. (1998) considered its deposition started at 5.2 Ma and Qiang et al. (2001) considered it started at 7.2 Ma. Another example of inconsistent age assignments refers to the age of the bottom of the Shilou (SL) section: it was first determined as 11 Ma (Xu et al., 2009), then 5.2 Ma (Anwar et al., 2015) and 8 Ma (Ao et al., 2016). Visual correlation of identified magnetic polarity intervals to the Geomagnetic Polarity Time Scale (GPTS), in the case of the lack of other independent chronostratigraphic constraints, can potentially produce different outcomes, especially when short polarity intervals are considered as geomagnetic subchrons, excursions and tiny wiggles, and even remagnetization (by the groundwater in this study). As a significant improvement in data analysis, the detection of astronomical signals in cyclostratigraphy has provided impressive advancements in stratigraphic correlations, by adjusting the magnetostratigraphic patterns through matching stratigraphic records to the Earth's orbital periodicities typical of the Milankovitch cycles (Anwar et al., 2015; Zhang et al., 2018, 2021a, 2021b, 2022).

## **S2 - Stratigraphic correlations from eastern to western CLP**

We compare the LL section to two other classical sections in the eastern and western edges of CLP, in a time interval spanning across the Mio-Pliocene boundary ([Supplementary Material Fig. 1](#)). Both Baode (BD) and Dongwan (DW) sections are located close to the mountains (for example, DW is located between Liupan Mts and West Qinling Mts which is close to Tibetan Plateau) as well as LL and SL (Hao and Guo, 2004; Zhu et al., 2008; Xu et al., 2009). These sections might be more affected by the seasonal cyclic variations of the Asian monsoon driven by tectonic uplift of a series of mountains during the Mio-Pliocene climate transition (Anwar et al., 2015; Zhang et al., 2021b; Zhang et al., 2022).

The lower part of the LL section, between 30–68 m, corresponds to the 38–69 m interval in the DW section and to of 60–117 m interval in the BD section, characterized by low MS values (average of  $38 \times 10^{-8} \text{ m}^3/\text{kg}$  for Liulin,  $64 \times 10^{-8} \text{ m}^3/\text{kg}$  for DW,  $59 \times 10^{-8} \text{ m}^3/\text{kg}$  for BD) and wide oscillations ([Supplementary Material Fig. 1a](#)). The upper part of the LL section between 0–30 m correlates to the interval of 12–38 m in DW and with interval of 49–60 m in BD, characterized by distinctly higher MS values (average of  $57 \times 10^{-8} \text{ m}^3/\text{kg}$  for LL,  $123 \times 10^{-8} \text{ m}^3/\text{kg}$  for BD,  $107 \times 10^{-8} \text{ m}^3/\text{kg}$  for DW) and lower amplitude oscillations. The MS variations for each section in the reconstructed time framework are shown in [Supplementary Material Fig. 1b](#). Two stages can be recognized across the LL section: the first stage at depth of 0 – 30 m represents the time interval of 5.5 – 4 Ma and the second stage at the depth of 30 – 68 m represents the time interval of 7 – 5.5 Ma. These data indicate that MS trend reflects a climate transition from lower values with stronger oscillations to higher values with slighter oscillations, while the trend of the coarse fraction ( $>63 \mu\text{m}$ ) content shows a corresponding transition at 30 m (ca. 5.5 Ma), from high values with wide variations in the lower part to low values with limited variations in the upper part ([Supplementary Material Fig. 1](#)). Both MS and GS trends suggest a transition for the Asian atmospheric circulation around the MPB boundary, a shift in the monsoon regime from the strengthening winter and weakening summer to the weakening winter and strengthening summer. This shift is synchronous with the DW section (Hao and Guo, 2004; Li et al., 2008), whereas it appears slightly younger (5.3 Ma) in the BD section (Zhu et al., 2008).

### **S3 - Wavelet analysis of magnetic susceptibility in the central CLP**

In the past few decades, many studies on successive red clay sections have been conducted through the CLP. Most chronology has been extensively studied and constrained through magnetostratigraphy ((Heller et al., 1982; Ding et al., 1998; Hao and Guo, 2004; Vandenberghe et al., 2004; Ao et al., 2016). In the main text, we compare the Jingchuan red clay section (Ding et al., 2001) from the middle part of CLP with LL and SL from eastern CLP. We show clearly the 1.2 Myr obliquity grand cycle observed in these sections. Further, here we integrated the other two well-constrained sections from the heart of CLP, to obtain a composite record of MS signal and Asian monsoon variability. These are Chaona (CN, Song et al., 2007, 2018) and Lingtai (LT, Ding et al., 1999; Sun et al., 2010), from the central CLP ([Supplementary Material](#)

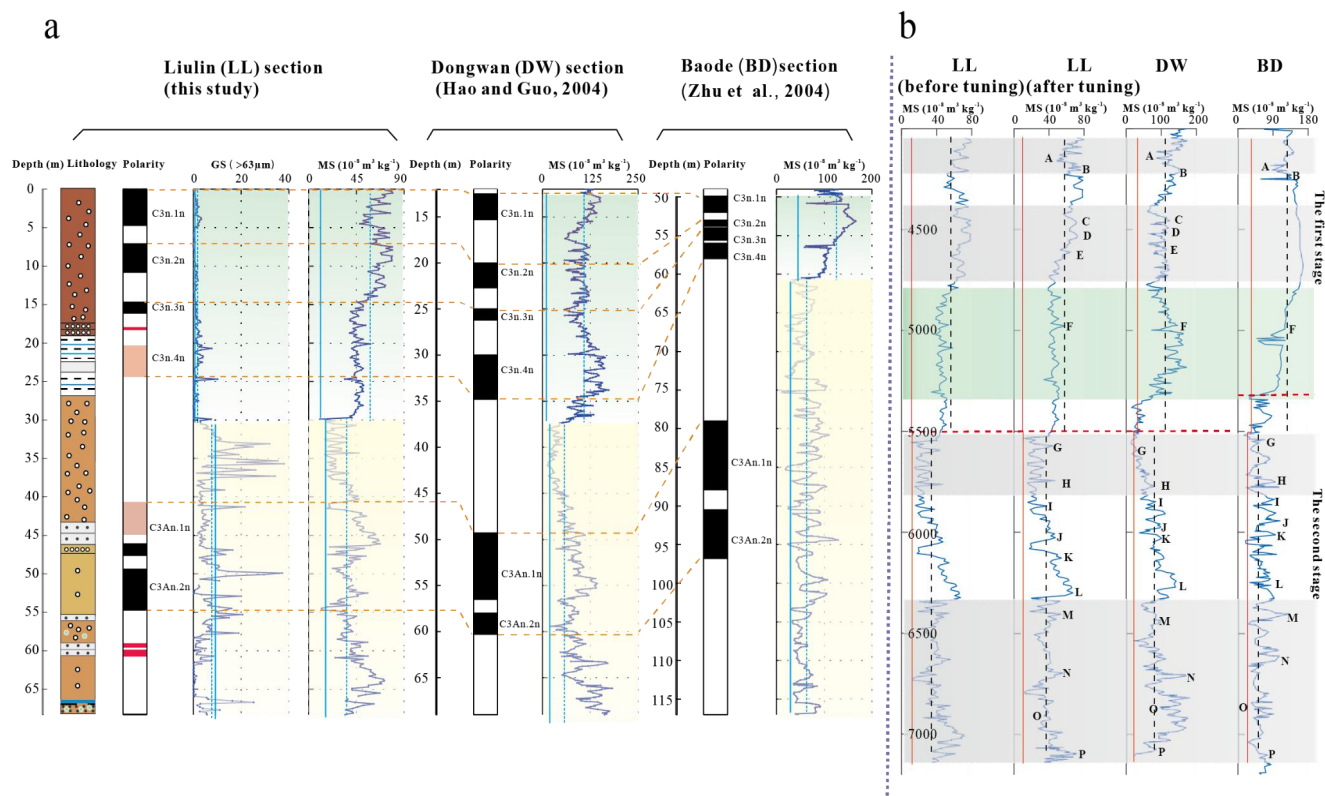
Fig. 2). The wavelet of MS from above sections, including a stacked MS, documented the amplitude-modulated 1.2 Myr band superimposed on the obliquity and eccentricity cycles for the first time discovery (Supplementary Material Fig. 3).

For stacked magnetic susceptibility (SMS) from LT, CN and JC sections in the central CLP, we started with aligning these records using a graphic correlation technique (Lisiecki and Lisiecki, 2002). Automated correlation algorithms (Lisiecki & Raymo, 2005) provided the first alignment criteria of objective technique to achieve a peak by peak correlation. Each alignment step was also evaluated by stratigraphic features to determine the quality of the matching and to distinguish noise or add tie points. We then chose the age model of one section (herein, LT) as a reference signal to correlate. Each MS record was aligned to the target and then averaged the normalized data at each time level to obtain the initial stacked data. After creating the initial stack, we tuned it to the 1.2-Myr-filtering obliquity as the prominent cycles were visually observed across all these sections (Supplementary Material Fig. 2). The process was iterative, for each result we monitored the spectral presence, if no good orbital cycles showed, we returned to the first step.

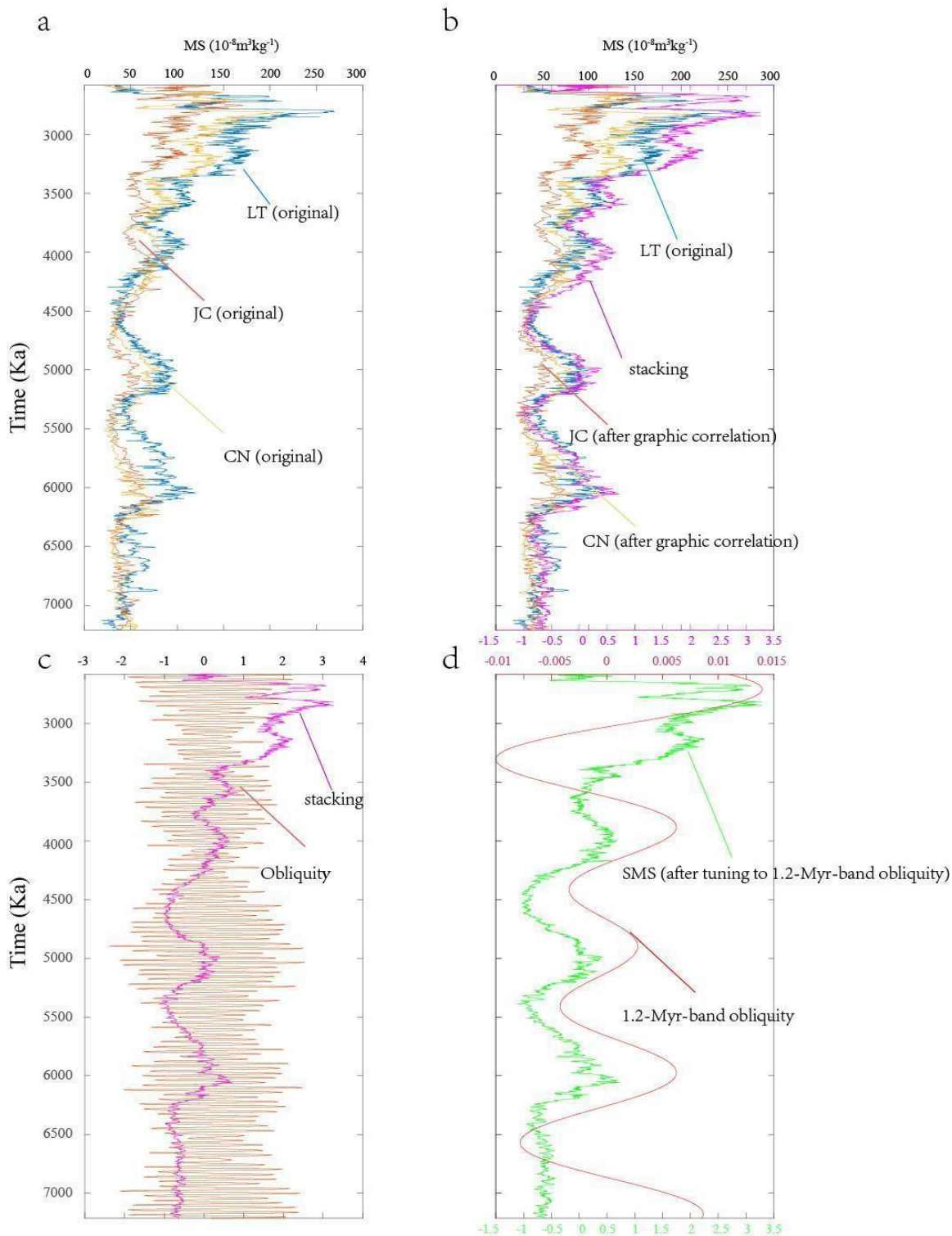
## References

- Ao, H., Roberts, A. P., Dekkers, M. J., Liu, X., Rohling, E. J., Shi, Z., An, Z. and Zhao, X., 2016. Late Miocene–Pliocene Asian monsoon intensification linked to Antarctic ice-sheet growth. *Earth and Planetary Science Letters* 444, 75–87.
- Ding, Z., Sun, J., Liu, T., Zhu, R., Yang, S. and Guo, B., 1998. Wind-blown origin of the Pliocene red clay formation in the central Loess Plateau, China. *Earth and Planetary Science Letters* 161, 135–143.
- Ding, Z., Xiong, S., Sun, J., Yang, S., Gu, Z. and Liu, T., 1999. Pedostratigraphy and paleomagnetism of a ~7.0 Ma eolian loess-red clay sequence at Lingtai, Loess Plateau, north-central China and the implications for paleomonsoon evolution. *Palaeogeography, Palaeoclimatology, Palaeoecology* 152, 49–66.
- Ding, Z., Yang, S., Hou, S., Wang, X., Chen, Z. and Liu, T., 2001. Magnetostratigraphy and sedimentology of the Jingchuan red clay section and correlation of the Tertiary eolian red clay sediments of the Chinese Loess Plateau. *Journal of Geophysical Research: Solid Earth* 106, 6399–6407.
- Hao, Q., Guo, Z., 2004. Magnetostratigraphy of a late Miocene-Pliocene loess-soil sequence in the western Loess Plateau in China. *Geophysical Research Letters* 31.
- Heller, F., Tung-sheng, L., 1982. Magnetostratigraphical dating of loess deposits in China. *Nature* 300, 431–433. <https://xs.scihub.ltd/https://doi.org/10.1038/300431a0>.
- Lisiecki, L. E., Lisiecki, P. A., 2002. Application of dynamic programming to the correlation of paleoclimate records. *Paleoceanography*, 17, 1–1.
- Lisiecki, L. E., Raymo, M. E., 2005. A Pliocene - Pleistocene stack of 57 globally distributed benthic  $\delta^{18}\text{O}$  records. *Paleoceanography*, 20.
- Song, Y., Fang, X., Chen, X., Torii, M., Ishikawa, N., Zhang, M., Yang, S. and Chang., 2018. Rock magnetic record of late Neogene red clay sediments from the Chinese Loess Plateau and its implications for East Asian monsoon evolution. *Palaeogeography, Palaeoclimatology, Palaeoecology* 510, 109–123.

- Song, Y., Fang, X., Torii, M., Ishikawa, N., Li, J. and An, Z., 2007. Late Neogene rock magnetic record of climatic variation from Chinese eolian sediments related to uplift of the Tibetan Plateau. *Journal of Asian Earth Sciences* 30, 324–332.
- Sun, Y., An, Z., Clemens, S. C., Bloemendal, J., Vandenberghe, J., 2010. Seven million years of wind and precipitation variability on the Chinese Loess Plateau. *Earth and Planetary Science Letters* 297, 525–535.
- Vandenberghe, J., Lu, H., Sun, D., van Huissteden, J.K., Konert, M., 2004. The late Miocene and Pliocene climate in East Asia as recorded by grain size and magnetic susceptibility of the Red Clay deposits (Chinese Loess Plateau). *Palaeogeography, Palaeoclimatology, Palaeoecology* 204, 239-255.
- Zhang, R., Kravchinsky, V. A., Anwar, T., Yue, L., Li, J. and Jiao, J., 2018. Comment on "Late Miocene-Pliocene Asian monsoon intensification linked to Antarctic ice-sheet growth" [*Earth Planet. Sci. Lett.* 444 (2016) 75-87]. *Earth and Planetary Science Letters* 503, 248–251.
- Zhang, R., Kravchinsky, V. A., Qin, J., Goguitchaichvili, A., Li, J., 2021a. One and a Half Million Yearlong Aridity During the Middle Eocene in North-West China Linked to a Global Cooling Episode. *Journal of Geophysical Research: Solid Earth* 126, e2020JB021037.
- Zhang, R., Wei, X., Kravchinsky, V. A., Yue, L., Zheng, Y., Qin, J., Yang, L., Ma, M., Xian, F., Gong, H., Zhang, Y., Liu, X., 2021b. "Tiny wiggles" in the late Miocene red clay deposits in the north-east of the Tibetan Plateau. *Geophysical Research Letters*, 48, e2021GL093962.
- Zhang, R., Li, X., Xu, Y., Li, J., Sun, L., Yue, L., Pan, F., Xian, F., Wei, X., Cao, Y., 2022. The 173-kyr obliquity cycle pacing the Asian monsoon in the eastern Chinese Loess Plateau from late Miocene to Pliocene. *Geophysical Research Letters*, 49, e2021GL097008.

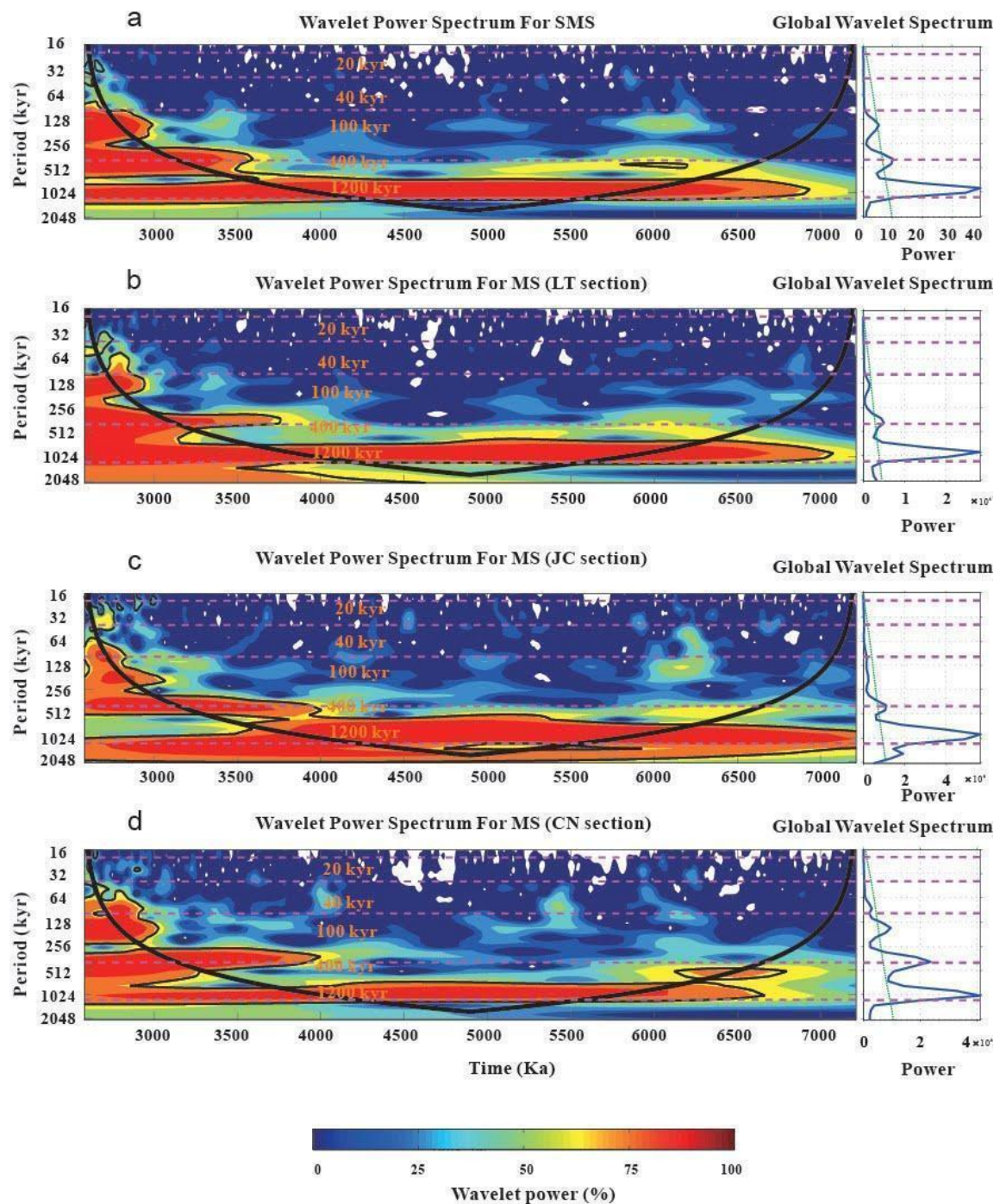


**Supplementary Material Fig. 1.** Comparison of polarity and magnetic susceptibility as a function of depth and age for the red clay sections. (a) LL: Polarity, grain size and MS of the LL red clay section. DW: Polarity and MS of the DW red clay section (Hao and Guo, 2002). BD: Polarity and MS of the BD red clay section (Zhu et al., 2008). The yellow dashed lines correlate the corresponding polarities of each section for mutual comparison. The green and yellow shadings indicate two comparable stages in changing MS for each section. Blue dashed lines represent the average values for each stage and blue solid lines represent the standard deviation. (b) Comparison of MS as a function of age for the red clay sections. LL: MS of the LL red clay section before tuning to eccentricity; MS of the LL red clay section after tuning to eccentricity. DW: MS of the DW red clay section. BD: MS of the BD red clay. The chronology for the DW and BD red clay sequences was obtained from magnetostratigraphy. The gray and white shadings indicate each comparable time interval of the three sections during which consistent variations can be observed. The red dashed lines denote the two stages reflecting different climatic conditions. The black dashed lines represent the average values of each stage and red solid lines represent the standard deviation. A–P shows consistent peaks from MS variations in the three sections during 7–4 Ma.



**Supplementary Material Fig. 2.** Illustration of stacking processing of magnetic susceptibility records from the central Chinese Loess Plateau. (a) Original magnetic susceptibility records before processing: blue—LT (Ding et al., 1999), yellow—JC (Ding et al., 2001), brown—CN (Song et al., 2007). (b) Magnetic susceptibility after graphic correlation and stacking. (c) Comparison of the initial stacking data and obliquity solution. (d) Stacked magnetic susceptibility after tuning to the 1.2-Myr-band obliquity.





**Supplementary Material Fig. 3.** Wavelet analysis of magnetic susceptibility records from the central Chinese Loess Plateau. (a) Wavelet spectrum of the Sacked magnetic susceptibility. (b) Wavelet spectrum of magnetic susceptibility from the LT section. (c) Wavelet spectrum of magnetic susceptibility from the JC section. (d) Wavelet spectrum of magnetic susceptibility from the CN section. The purple dashed line marks the orbital period. The thin black contour encloses regions of greater than 95% confidence for a red-noise process with a lag coefficient of 0.8. The thick black contour indicates the cone of influence. The global wavelet spectrum to the right illustrates the mean red noise spectrum, as indicated by the green dashed line. The color bars correspond to wavelet power.